FINAL REPORT

Microchannel Heat Sink with Micro Encapsulated Phase Change Material (MEPCM) Slurry

Funded by: ONR N00014-06-1-1120

Program Manager: Dr. Mark Spector
Code 331

Period of performance: September 8, 2006 – May 31, 2009.

Contributors:

Dr. Louis Chow (Principal Investigator)
Dr. Jian-hua Du
Amit Gupta
Krishna Kota
Dr. Ranganathan Kumar
Sarada Kuravi

REPORT DOCUMENTATION PAGE

Form Approved
OMB No. 0704-0188

1. REPORT DATE *(DD-MM-YYYY)*	2. REPORT TYPE	3. DATES COVERED *(From - To)*
31-08-2009	Final	08-Sep-2006 to 31-May-2009

4. TITLE AND SUBTITLE
Microchannel Heat Sink with Micro Encapsulated Phase Change Material Slurry

5a. CONTRACT NUMBER

5b. GRANT NUMBER
N00014-06-1-1120

5c. PROGRAM ELEMENT NUMBER

6. AUTHOR(S)
Chow, Louis (Principal Investigator); Du, Jian-hua; Gupta, Amit; Kota, Krishna; Kumar, Ranganathan; and Kuravi, Sarada (main author)

5d. PROJECT NUMBER

5e. TASK NUMBER

5f. WORK UNIT NUMBER

7. PERFORMING ORGANIZATION NAME(S) AND ADDRESS(ES)
University of Central Florida
Office of Research and Commercialization
12201 Research Parkway, Suite 501
Orlando, FL 32826

8. PERFORMING ORGANIZATION REPORT NUMBER
UCF-MMAE-09-01

9. SPONSORING/MONITORING AGENCY NAME(S) AND ADDRESS(ES)
Office of Naval Research
875 North Randolph Street
Arlington, VA 22203-1995

10. SPONSOR/MONITOR'S ACRONYM(S)
Spector, Mark/ONR 331

11. SPONSOR/MONITOR'S REPORT NUMBER(S)
None

12. DISTRIBUTION/AVAILABILITY STATEMENT
Approved for Public Release; distribution is Unlimited

13. SUPPLEMENTARY NOTES
None

14. ABSTRACT

High heat flux removal from devices such as Insulated-Gate Bipolar Transistor (IGBT) and Monolithic Microwave Integrated Circuit (MMIC) will be important for future Navy ships. Micro encapsulated phase change material (MEPCM) slurry was used as a heat transfer fluid inside a microchannel instead single phase fluid. Presence of phase change material increases the effective heat capacity of the fluid. The performance of encapsulated phase change material (EPCM) slurry flow in microchannels was investigated using the effective specific heat capacity method. Lattice Boltzmann method was used to simulate the particle paths when the duct shape has different aspect ratios. For higher concentrations, a shear induced migration model was used to simulate the nonhomogeneous particle distribution. Results of the model were used to solve the temperature distribution inside the channels. Parametric study was carried out with water and PAO as base fluids in microchannels of two different widths, 101 μm and 25 μm. Parameters varied include particle concentration, inlet temperature of the fluid, melting range of PCM and base heat flux.

15. SUBJECT TERMS
Phase Change Materials; microchannel cooling; slurry flow; high heat flux

16. SECURITY CLASSIFICATION OF:			17. LIMITATION OF ABSTRACT	18. NUMBER OF PAGES	19a. NAME OF RESPONSIBLE PERSON
a. REPORT	b. ABSTRACT	c. THIS PAGE			Chow, Louis
U	U	U	UU	82	19b. TELEPHONE NUMBER *(Include area code)* 407-823-3666

TABLE OF CONTENTS

ABSTRACT

High heat flux removal from devices such as Insulated-Gate Bipolar Transistor (IGBT) and Monolithic Microwave Integrated Circuit (MMIC) will be important for Navy ships in future applications. Micro encapsulated phase change material (MEPCM) slurry was used as the heat transfer fluid inside a microchannel instead single phase fluid in present study. Presence of phase change material increases the effective heat capacity of the fluid. To enable the application of using MEPCM slurry in microchannel cooling, three research tasks were identified; namely, clogging experiments (Task 1), heat transfer experiments (Task 2) and numerical modeling (Task 3). While prior reports have described the efforts in Tasks 1 and 2 and the corresponding results, the focus of this report is on Task 3 involving numerical modeling of EPCM slurry in microchannels.

Particle migration inside microchannels of different aspect ratios was simulated using the lattice Boltzmann method (LBM). Channels of aspect ratios from 1 to 4 have been used for modeling the geometry. The particle size to the smallest dimension of the channel ratio is taken to be 1/10 and the particle concentration is less than 0.5% for all cases simulated. Simulations show that these particles migrate to preferred locations in the channel, known as equilibrium locations, and these depend on Re and aspect ratio of the channel. For aspect ratio 2 and higher, particles form an inner ring that moves away from the wall as Re is increased further. An outer ring is formed, which moves closer to the walls as Re is increased. The location of these inner and outer rings is strongly dependent on the Reynolds number of the flow.

For modeling higher concentrations, a shear induced migration model based on macroscopic constitutive equations was employed and was used to simulate the nonhomogeneous particle distribution inside the microchannel. The particle distribution was modeled using the diffusive flux model and the results were used to solve the temperature profile. In order to investigate the effect of particle migration, the thermal results obtained with and without including the particle migration were compared. It was

found that for the parameters considered, the difference in slurry performance prediction assuming nonhomogeneous and homogeneous distribution is not significant.

For parametric study, the three dimensional flow inside the microchannels was solved including the microchannel wall/fin effects and developing flow in manifold microchannels. A constant inlet velocity and temperature were assumed along with constant heat flux condition at the base of the microchannel. Thermal performance of water and poly-alpha-olefin (PAO) based slurries were analyzed in microchannels of width 101 μm and 25 μm. Pressure drop of both slurries is higher compared to the pure fluid as expected. Heat transfer coefficient of slurry is lower compared to water because of lower thermal conductivity in microchannels of width 101 μm. In case of 25 μm wide channels, water based slurry performed better compared to water due to faster development of temperature profile. It was found that PAO slurry performs better in both channels.

PROGRESS STATEMENT SUMMARY

The performance of encapsulated phase change material (EPCM) slurry flow in microchannels was investigated using the effective specific heat capacity method. Lattice Boltzmann method was used to simulate the particle paths when the duct shape has different aspect ratios. For higher concentrations, a shear induced migration model was used to simulate the nonhomogeneous particle distribution. Results of the model were used to solve the temperature distribution inside the channels. Parametric study was continued with water and PAO as base fluids in microchannels of two different widths, 101 μm and 25 μm. Parametric study was done by varying parameters such as particle concentration, inlet temperature of the fluid, melting range of PCM, base heat flux and base fluid.

.

Nomenclature

A	Aspect ratio
A_b	Area of base, m^2
a	Particle radius, m
B	Width of the channel, diameter of the tube, m
Bi	Biot number
Bi_p	Biot number of particle
c	Volume concentration of MEPCM particles in slurry
c_m	Mass concentration of MEPCM particles in slurry
$c_{p,b}$	Specific heat of bulk fluid, J/kg.K
$c_{p,f}$	Specific heat of fluid, J/kg.K
$c_{p,p}$	Specific heat of MEPCM particle, J/kg.K
$c_{p,pcm}$	Specific heat of PCM, J/kg.K
D	Hydraulic diameter, m
d, d_p	Particle diameter, m
e	Magnitude of shear rate, 1/s
e_i	Phase space vector along link 'i', m/s
f	Enhancement factor
f_i	Particle distribution function
G	velocity gradient, s^{-1}
G'	effective velocity gradient, s^{-1}
H	Height of the channel, Shortest dimension of rectangular channel, m
H_m	Height of manifold in simulation domain, m
h	Heat transfer coefficient, $W/m^2.K$
h_r	Heat transfer coefficient ratio, = $h_{slurry}/h_{base\ fluid}$
h_{sf}	Latent heat of fusion, J/kg
k	Thermal conductivity, W/m.K
k_b	Thermal conductivity of bulk fluid, W/m.K
k_{eff}	Effective thermal conductivity of bulk fluid, W/m.K
k_f	Thermal conductivity of fluid, W/m.K

k_p	Thermal conductivity of MEPCM particle, W/m.K
k_{pcm}	Thermal conductivity of PCM, W/m.K
L	Length of the channel, m
L_{ss}	Length of the channel for fully developed particle distribution profile, m
$\dot{m}$	Mass flow rate inside the microchannel, kg/s
Nu	Nusselt number
n	Unit normal
Pe	Peclet number
PF	$\Delta P_{base\ fluid}/\Delta P_{slurry}$, when $h_{slurry} = h_{base\ fluid}$
Pr	Prandtl number
p	Pressure, psi
p_{in}	Pressure at the inlet, psi
p_{out}	Pressure at the outlet, psi
K_c, K_η	Phenomenological constants
Q	Heat supplied, W
q	Heat flux, W/cm^2
q_w	Constant wall heat flux, W/cm^2
R	Radius (m)
Re	Reynolds number
Re_D	Reynolds number for a circular channel
Re_p	Particle Reynolds number = $Re_{max}(a/H)^2$
R_p	Radius of MEPCM particle, m
r	Space coordinate
r	Radial coordinate, m
r_p	Solid liquid interface radius, m
T	Temperature, K
T_1	Lower melting temperature, K
T_2	Higher melting temperature, K
T_{in}	Temperature at heat sink inlet, K, Temperature at microchannel inlet, K
T_{Mr}	Melting range = T_1-T_2, K
T_m	Melting temperature, K

T_{out}	Temperature at heat sink outlet, K, Temperature at microchannel outlet, K
T_w	Wall temperature, K
$T_{w,max}$	Maximum wall temperature, K
t	Time, s, Time coordinate
t_{base}	Base of microchannel, m
t_{ch}	Half of microchannel width, m
t_{res}	Residence of MEPCM particle inside the channel, s
t_s	Stokes time, s
t_w	Half of Microchannel wall thickness, m
U	Velocity distribution, m/s
U_{avg}	Average velocity of the flow, m/s
U_{eff}	Effective velocity on the particle, m/s
U_0	Maximum velocity of the flow, m/s
$\boldsymbol{u}, \bar{u}$	Velocity vector, m/s
u	Velocity in x direction, m/s
V_{HS}	Volumetric flow rate at the heat sink inlet, m^3/s
V_r	Radial velocity of the particle, m/s
V_z	Axial velocity of the particle, m/s
v	Velocity vector
v	Velocity in y direction, m/s
W	Half channel width, m
w	Velocity in z direction, m/s
x,y,z	Spatial coordinates
x	Distance from channel symmetry, m
x	Space vector
Y	Non-dimensional coordinate along the 'y' axis
Z	Non-dimensional coordinate along the 'z' axis
ΔP	Pressure drop, psi
ΔP_r	Pressure drop ratio, $\Delta P_{slurry}/\Delta P_{basefluid}$
ΔT_{bulk}	Bulk temperature rise, T_{out}-T_{in}, K
Δt, δt	Time step, s

ΔV_z	Axial relative velocity of the particle, m/s
δx	Grid spacing, m
p	Pressure, Pa
Pe	Peclet number

Greek symbols

α	Thermal diffusivity, m^2/s
α_p	Thermal diffusivity of MEPCM particle, m^2/s
α_f	Thermal diffusivity of fluid, m^2/s
γ	Shear rate, 1/s
κ	Velocity gradient, s^{-1}
θ	Non-dimensional temperature = $(T - T_m)/ (q_w R_d/k_{bulk})$
μ,η	Dynamic viscosity (Pa.s)
μ_b	Dynamic viscosity of bulk fluid, Pa.s
μ_f	Dynamic viscosity of fluid, Pa.s
μ_p	Dynamic viscosity of MEPCM particle, Pa.s
ν	Kinematic viscosity, m^2/s
ρ	Density, kg/m^3
ρ_b	Density of bulk fluid, kg/m^3
ρ_f	Density of fluid, kg/m^3
ρ_p	Density of MEPCM particle, kg/m^3
τ	Time constant, s
φ	Particle volume concentration

Subscripts

b	Bulk
d	Duct
eff	Effective
exit	Exit/Outlet
eq	Equilibrium
f	Fluid

i	Index
inlet	Inlet
l	Liquid phase
m	Mean
max	Maximum
p	Particle
pcm	PCM
s	Solid phase
w	Wall

SECTION 1: TECHNICAL OBJECTIVES

We have identified three key fundamental issues in the application of micro encapsulated PCM slurries in microchannel heat sinks. Three tasks are proposed which will improve our understanding of the issues, resulting in solutions to potential problems. There have not been any experiments reported so far that use PCM slurries in channels of less than 3.14 mm size. Hence it forms an interesting and important aspect to perform experiments on microchannel heat sinks with channel sizes between 100 μm and 500 μm and filled with MEPCM slurry with different particle sizes and concentrations. Also, the validity of the existing modeling work is questionable and further theoretical investigation is needed. Two different experiments, one for observing the clogging and the other for finding the pressure drop and thermal performance of slurry will be performed. The numerical modeling will include the modeling of particle distribution in microchannels and thermal performance based on the non homogeneous distribution.

SECTION 2: TECHNICAL APPROACH

For observing clogging inside the microchannel a microfluidic channel test section fabricated at UCF were employed. These channels are 100 μm in height, 500 μm in width and 6 mm in length. Water will be used as base fluid and MEPCM particles with n-eicosane as phase change material will be used for experiments. This experiment will be done with particle diameters less than 30 μm and for different Reynolds numbers.

For the heat transfer and pressure drop experiments, a custom fabricated SA-2 cooler from Micro Cooling Concepts, Inc.® will be used. These channels are 100 μm in width, 500 μm in height and 1 mm in length. In these experiments, heat transfer and pressure drop across a SA-2 cooler using MEPCM slurry as the working fluid will be analyzed under different concentrations and Reynolds number and the results will be compared with those of using water in the same test setup.

Since MEPCM slurry flow in microchannels is a kind of suspension flow of particles in fluid under motion, the particle-particle, particle-wall and particle-fluid interactions are important. Lattice Boltzmann approach is a realistic method to simulate suspension flows as it accounts for all the forces is not as computationally intense as molecular level dynamic simulations. The lattice Boltzmann method (LBM) is based on a microscopic model but is used to model macroscopic fluid properties. This method is used for simulating the particle distribution inside the microchannel. A macroscopic model that simulates the particle distribution along the channel based on the diffusive flux model will be used for simulating the particle distribution inside the microchannels. These results will be used for analyzing the thermal performance of slurry. For this purpose, using the simulation results shear-induced hydrodynamic model for the MEPCM slurry in microchannels, a volume averaged macroscopic model on heat transfer will be developed based on continuum energy transport equation. The effective thermal conductivity will be calculated based on the concentration of the MEPCM particles. Heat absorption delay

will be considered by solving the heat transfer process in the particles. The solution will consider the melting temperature range and the possible effect of the sensible heat of PCM on heat transfer. Heat transfer coefficient will be calculated based on the liquid and particle velocities obtained from the hydrodynamic simulation. Heat absorption will be considered as a heat sink term in energy equation for liquid. The analysis will be compared with the experimental results.

SECTION 3: ANNUAL PROGRESS

3.1 Introduction

Tuckerman and Pease in 1981 demonstrated a microchannel heat sink that removes 790 W/cm^2 with 71°C temperature increase at 600mL/min flow rate [1]. The heat sink was numerous small channels and fins arranged in parallel directly fabricated in a silicon substrate and had direct circulation of water. It is so compact that heat is efficiently carried from the substrate into the coolant because of its inherently small passageways and a very large surface-to-volume ratio. It has already been proved that the use of microchannel heat sinks has numerous advantages compared to macroscale flow channels. Tuckerman and Pease predicted that single-phase forced convective cooling in microchannels should be feasible for circuit power densities of more than 1000 W/cm^2. However, the heat sink had quite a large pressure drop of 200kPa with plain microchannels and 380kPa with pin fin enhanced microchannels. For single phase cooling, the coolant temperature will increase in the flow direction as it acquires heat, which leads to non-uniform temperature distribution on the chips. In order to keep the temperature of devices such as semiconductors and lasers to be cooled within a few degrees Celsius, a very large mass flow rate is needed, resulting in high pressure drop across the microchannels, even prohibitively high sometimes, which need a large pump in the system and consume a large amount of pumping power. Boiling heat transfer inside microchannels has been investigated to utilize latent heat of vaporization [2]. However, the increased pressure drop and associated pressure fluctuation, and wall temperature fluctuation in microchannels hinder the application of convective boiling in microchannels in electronic cooling. Possible dry-out at relatively low heat flux compared with its single-phase flow counterpart prevents two-phase flow in microchannels to be used in cooling of high heat flux electronics [3].

In applications where high temperature variation and large pressure drop are unacceptable, manifold microchannel heat sink (MMC) [4] is shown to be an effective way in reducing the pressure drop and significantly reducing the temperature variation.

This is possible because of the presence of multiple short channels in the MMC heat sinks distributed along the length of the device that needs to be cooled. The MMC heat sink (figure 1) features many inlet and outlet channels alternating at a periodic distance along the length of the microchannel [5]. The flow enters the microchannels from the manifold inlet channel, splits and flows through the microchannels, then exits to the manifold outlet channel. This pattern is repeated along the length of the chip. These channels are shown to have small pressure drop compared to traditional microchannels with little effect on thermal resistance.

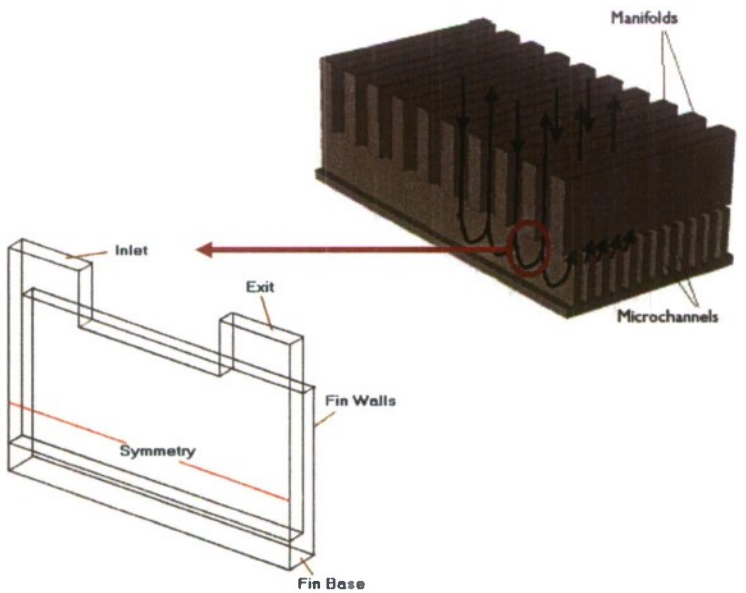

Figure 1: MMC heat sink geometry

The intention of this work is to cool the high-power devices that produce high heat fluxes and require continuous heat removal under near isothermal condition. This project proposes to make use of the latent heat of a microencapsulated solid-liquid phase-change material (MEPCM) as working fluid to increase thermal capacity of the coolant. PCM-filled particles will be well mixed in the liquid. The use of the two-component fluid would provide additional thermal capacity from the latent heat associated with the solid-liquid phase change.

The PCM in the microcapsules can be selected to melt and freeze at the desired temperature. By microencapsulating the PCM, the core material remains separated from the carrier fluid, thus preventing its agglomeration or deposition within a system. In 1983, Colvin et al. [6] at Triangle Research and Development Corporation (TRDC) in Research Triangle Park, North Carolina, began a long series of pioneering investigations that have resulted in microPCMs of high strength enough to expose to high pressure and external media. For the first time, TRDC investigators demonstrated that paraffinic PCMs could be successfully microencapsulated, suspended in water and pumped in a closed-loop system [7]. Significant improvements were made by TRDC regarding the longevity of the microPCM coolants, which outlasted the bearings in the circulating pumps through over 100,000 thermal cycles [6].

In MEPCM slurries, the materials used for the core and the shell are selected compatible and the shell material is selected compatible with the carrier fluid. Particle diameters typically range from 6 μm to 50 μm. The shell can be less than one micron thick. Upon heat absorption, the core material in the particles melt, changing from solid to liquid and the resulting volumetric expansion of about 12 to 15% is accommodated by particle's flexible wall. Though the density of the PCM is usually not identical to that of the carrier fluid, the thickness of the shell wall can be adjusted so that nearly neutrally buoyant suspension can be obtained with relative homogeneity. Particle concentrations (loadings) can range up to 35% solids (weight/weight) depending on the nature of the carrier fluid. In addition, the degree of uniformity may be increased by adding a suitable dispersing agent [6]. Figure 2 shows the cross section of a single microPCM particle, while figure 3 illustrates a scanning electron microscope image of typical microencapsulated PCM particles.

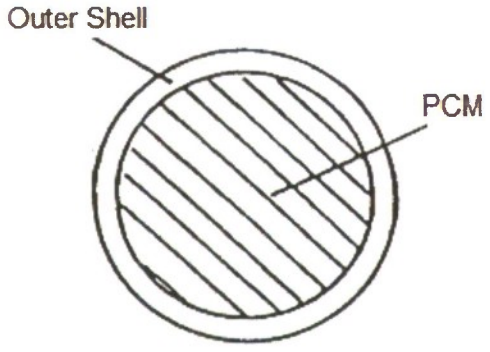

Figure 2: Cross section schematic of a single MEPCM

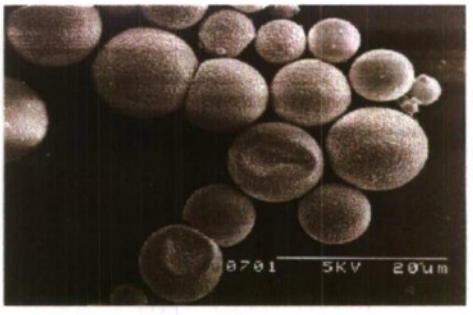

Figure 3: SEM image of microencapsulated PCM Particles

A sample of PCM slurry was made at University of Central Florida with water as base fluid and octadecane as PCM. The particle size is around 0.1 μm and the shell thickness is around 5nm. It is prepared by emulsification process where a surfactant (shell material) is first dissolved in the base fluid and is then heated to a temperature greater than the melting point of PCM while stirring continuously. Later the PCM is added to the mixture to carry out the emulsification. The formation of the encapsulated PCM was confirmed using the Tyndall's effect. This involves the scattering of a laser beam as it passes through the emulsion due to the presence of encapsulated particles (figure 4). Pure water itself cannot scatter the laser beam. Figure 5 shows the measured size distribution of the sample with a diameter distribution at around 0.06 μm to 0.125 μm. Figure 6 shows the DSC curve of the sample. A slightly broader peak at around 20 ^{0}C is due to the phase change of PCM. It can be observed that the phase change peak is around 20 ^{0}C and not between 28 ^{0}C to 30 ^{0}C, typical to octadecane which is probably induced by the small size, where the surface effect is much more significant than that at micro scale.

The proposed working fluid is a kind of two component slurry that consists of the MEPCMs mixed homogeneously in a conventional sensible heat transfer fluid. The assumption of homogeneous Newtonian fluid is valid for the slurry flow mechanisms for

the particle loading range of 0-25% volume [8]. The effective specific heat during phase change given by [6]:

$$c_{p,eff} = \overline{c}_p + \frac{xc_m h_{sf}}{\Delta T_{bulk}} \tag{1}$$

where $\overline{c}_p$ is the weighted average specific heat given by $\overline{c}_p = (1-c)c_{pwf} + cc_{pcm}$, x is the fraction of particles undergoing phase change, c is the loading fraction, ΔT is the temperature rise of fluid, h_{sf} is the latent heat of melting of PCM, c_{pwf} is the specific heat of working fluid and c_{pcm} is the specific heat of solid PCM. As an example, assuming the PCM has completely change its phase from solid to liquid at the exit of channels (x=1), working fluid as water, the loading fraction is 0.2 (c = 0.2), latent heat of PCM as 250kJ/kg, c_{pcm} as 2 kJ/kgK and ΔT as 3°C, the effective specific heat will be 21 kJ/kg.K. This implies that the specific heat is increased by about 5 times with the presence of MEPCM.

Figure 4: Light scattering of nanoPCM in right jar; left jar has water

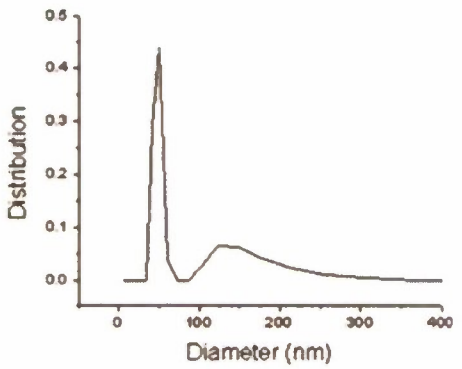

Figure 5: Size distribution of NEPCM particles in slurry sample

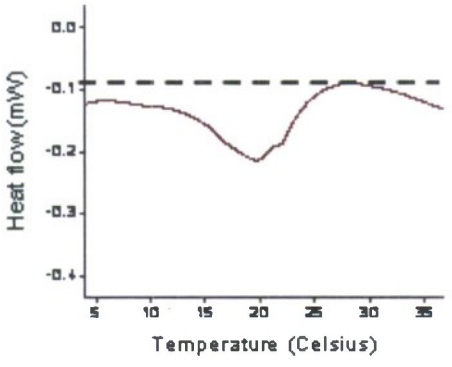

Figure 6: DSC curve of NEPCM slurry

Colvin and Mulligan[9] have reported that with increase of specific heat of fluid by PCM slurry, for the same temperature rises, the flow rate can be reduced to one-tenth (or by 90%) and the pumping power to one-hundredth (or by 99%) for a given heat flux. Similar reductions in pumping power have also been reported by Goel et al. [10]. MEPCM can greatly enhance the performance of a microchannel heat sink by providing higher convective heat transfer coefficients, better axial temperature uniformity, and reduced coolant flow rate requirements.

We proposed to use MEPCM slurry as the heat transfer fluid inside the microchannels instead of only liquid for the following advantages:

- High rate of heat transfer per unit volume due to the ratio of surface area to volume of microchannels leads to capability of removal of high heat flux.
- The presence of MEPCM particles in the fluid increases the overall heat capacity and hence the mass flow rate can be significantly decreased while maintaining a near isothermal condition at the heat source.
- The reduction in mass flow rate would decrease the overall pressure drop, resulting in a small pump and less power consumption for fluid circulation.
- The Microencapsulated PCM shows a higher thermal cycling resistance.

3.1a Related Work

The use of phase change materials in liquids has been studied extensively for performance enhancement in conventional size channels [8, 12]. Colvin et al. [11] reported specific heat increase up to five times and heat transfer coefficient increase of up to 2.8 times in flows of MEPCM suspension. Increase in convective heat transfer coefficient partially comes from the increase in effective specific heat due to the latent heat of the MEPCM. Since, $Nu \propto \mathrm{Pr}^{0.4}$, the convective heat transfer coefficient for a single-phase fluid can be described in terms of thermal conductivity and specific heat by following relation:

$$h \propto k^{0.6} c_p^{0.4} \tag{2}$$

If the latent heat is viewed as a form of specific heat, the increase in effective specific heat, which includes the effect of latent heat, can lead to an increase in the heat transfer coefficient. The effective thermal conductivity of static dilute suspension can be evaluated from Maxwell's relation [12]:

$$k_b = \frac{2 + k_p / k_f + 2c(k_p / k_f - 1)}{2 + k_p / k_f - c(k_p / k_f - 1)} \tag{3}$$

Sohn and Chen [13] showed that the thermal conductivity of solid-liquid suspensions increased effectively in a laminar flow because of the effects of micro-convection around solid particles and particle-to-particle interaction. It was found that the degree of the enhancement of thermal conductivity increases as particle diameter increases. For particles of diameter smaller than 100 μm, this enhancement can be negligible. An associated heat transfer enhancement is therefore believed to be marginal compared to that related to latent heat [14].

The primary parameter that affects the heat transfer enhancement of the phase change slurry flow is the bulk Stefan number [8]. It is defined as the ratio of the sensible heat capacity of the suspension to its latent heat capacity. For the constant heat flux condition, it can be expressed as [8]:

$$Ste_b = \frac{c_{pe}(q_w r_d / k_b)}{cL(\rho_p / \rho_b)} \tag{4}$$

where q_w is the wall heat flux, r_d is the channel radius, ρ_p and ρ_b are the density of the particle and the bulk fluid. Experimental investigation demonstrated [10] that, the wall temperature rise decreases with the decrease in Stefan number for the boundary condition of constant wall heat flux. From the definition of the Stefan number, it is clear that for given fluid and phase change materials, its value depends on the channel size and concentration. Thus for best cooling results, a low Stefan number should be maintained as far as possible by either by increasing the microcapsule concentration or by reducing the duct radius.

There are very limited experimental investigations on heat transfer of MEPCM slurry. Goel et al. [10] conducted an experimental study for cases of flow in a circular tube of 3.14mm inner diameter with a constant heat flux boundary condition. Yamagishi et al.[15] experimentally investigated the hydrodynamics and heat transfer characteristics of slurry containing microencapsulated phase change material for use as a heat transfer fluid in a circular tube of 10mm with uniform heat flux condition. Goel et al's experiment is the smallest tube size we can found up to now.

As mentioned above, small tube size can improve cooling performance for PCM slurry flow. Tao et al. [16] proposed a heat sink design that contains a 3D micro/nano network and liquid fluid mixed with nanosize phase change materials (NPCMs). Hao and Tao [17] developed a numerical model to investigate the heat transfer characteristics of PCM slurry in microchannels. The model was based on the continuum model for both the carrier fluid and PCM particles. The interaction of momentum between liquid and solid is coupled based on the empirical correlation for packed beds or fluidized beds, depending on the concentration of the slurry. The authors assumed local thermal equilibrium for both liquid and solid. Separate volume-averaged energy equations were written for the

liquid and PCM particles. Two energy equations are coupled by an interfacial heat transfer coefficient estimated based on Wakao and Kaguei's relation. They compared their simulation [18] with experimental result for a microencapsulated PCM suspension flow in a 3mm diameter tube [10].

In order to reduce the temperature rise for removal of high heat fluxes, high loading is expected to increase the overall specific heat of in working fluid. Hydrodynamic and heat transfer characteristics of microencapsulated PCM slurry in microchannels will be quite different from those of dilute slurry in conventional size channels. There are some fundamental issues to be addressed for understanding flow and heat transfer of PCM slurry in the microchannel as a first step towards application. The numerical and experimental work that has been performed till now is described in the next two sections.

3.2 Particle Migration in Suspension Flows

Last year, the formulated LBM code was used to simulate the particle paths when the duct shape has different aspect ratios and few results were presented. This year, the simulations were continued and more results are presented after a brief introduction to particle migration and LBM methodology.

Most of the numerical models simulating MEPCM slurry flows assumed homogeneous distribution of particles. The model proposed by Tao et al. [16] use fluidized bed correlations to solve the particle distribution and is derived only for two-dimensional flows. So it is important to understand the behavior of particles in microchannels where the length of the channel is not enough for the particle distribution to be fully developed.

When a slurry or suspension flow inside a channel, it was observed by many researchers that the particles tend to migrate and the flow becomes nonhomogeneous even though it is homogeneous at the inlet. This effect has been first observed by Siegre and Silberberg [19] and noted that a neutrally buoyant particle tends to migrate to an equilibrium position approximately at 0.6r, at low Re, where r is the pipe radius. This effect is known as Siegre and Silberberg effect or tubular pinch effect (figure 7). The mechanisms suggested for particle migration in concentrated suspensions include hydrodynamic interactions, electrostatic interaction, and other surface interactions that become important as the particles are close.

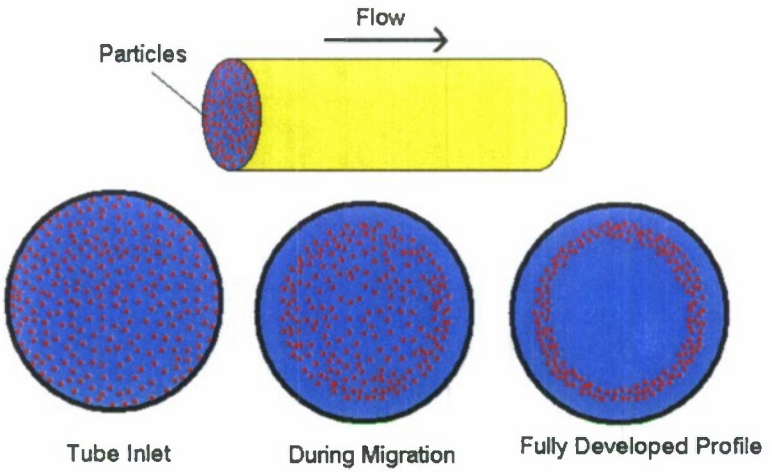

Figure 7: Particle distribution over a cross section of tube

There has been growing interest in the flow of solid suspension and the particle distribution recently. In cases where Brownian motion is negligible, the migration of particles has been attributed to the presence of inertial forces. However, under vanishingly small particle Reynolds numbers, inertial forces are not dominant and the migration of particles depends purely on the shear-induced forces. Most studies on particle migration in semi-concentrated or concentrated suspension have been focused on the cases of vanishingly small particle Reynolds number, Re_p [20-30]. These models are based on different simulation techniques such as Stokesian dynamics, Lattice Boltzmann methods, dissipative particle dynamics and the Lagrange multiplier fictitious domain method.

3.2a Simulation of Particle Distribution Using LBM

Lattice Boltzmann (LB) methods belong to the family of mesoscopic methods. Each conservation law is related to a microscopic quantity which is conserved exactly by the collision operator of the evolution equation. The evolution equation describes the dynamics of distribution functions moving with discretized velocities between the nodes of the computational grid. The method proposed by Ladd [31, 32] for simulation of particulate suspensions using lattice Boltzmann method (LBM) has been used in the current project to simulate the particle distribution. One of the important features of the

present method is that the computational cost scales linearly with the number of particles in the domain. In the lattice Boltzmann method of simulating such particulate suspensions, the discrete-velocity models of the fluid combine the features of a fully molecular simulation of both solid and liquid phases, at the same time being orders of magnitude faster than computationally intensive solutions of the Navier-Stokes equations. As compared to Navier-Stokes based solvers, lattice Boltzmann simulations are fast, flexible and simple.

The Boltzmann's kinetic equation is a well established mathematical model of a fluid at the microscopic level which describes the evolution of the single particle distribution function. The problem is to determine the time evolution of the particles with velocity $\mathbf{v}$ around the space-time point $(\mathbf{r},t)$ given as $f(\mathbf{r},\mathbf{v},t)$. The one-particle distribution function $f_i(\mathbf{r},t)$ describes the number density of particles at a particular node of the lattice $\mathbf{r}$ and time t with velocities given by $\mathbf{e}_i$. The equation for the particle distribution function using the lattice BGK (LBGK) equation is given by:

$$f_i(\mathbf{x}+\mathbf{e}_i\delta t, t+\delta t) - f_i(\mathbf{x},t) = -\frac{(f_i - f_i^{eq})}{\tau} \tag{5}$$

where f_i^{eq} is the equilibrium distribution of particles moving in direction 'i'.

The density per node and the macroscopic momentum flux are defined in terms of the particle distribution functions by:

$$\rho = \sum_i f_i \quad ; \quad \rho\mathbf{v} = \sum_i f_i \mathbf{e}_i \tag{6}$$

The details of the model can be found in [33, 34]. LBM was used to simulate distribution of particles in a channel over a period of time.

3.2b. Results Using LBM

In the current simulations, particle size is varied between d=9.6δx and d=16.4δx and the duct cross-section varies from 10d×10d to 10d×40d for a range of aspect ratios between 1 and 4. The length of the duct is kept constant at $20d$ for all the simulations. As the lattice Boltzmann equation is weakly compressible, simulations at higher Reynolds number were conducted with particles of size d=16.4δx and with low viscosity fluids. Secondary flow is known to emanate from the corners of the duct and can propagate into the main flow [35]. The magnitude of velocities in the region of secondary flows is proportional to the velocity of the flow. At high Re, to minimize the effect of the secondary flows simulations were conducted with low viscosities. The Reynolds number used in the current simulations is based on the shorter side of the channel cross-section, and is defined as $\mathrm{Re} = \rho H U_{avg} / \mu$.

Results in square microchannels (aspect ratio = 1)

Simulations were conducted to validate the results for a square duct with 16-20 particles distributed randomly in the channel. Figure 8 compares the randomly assigned initial particle positions with the positions after migration was found to be completed, around $t=10{,}000t_s$ for Re=100. Here t_s is the Stokes time and is given by $t_s=d/2U_{avg}$. It can be observed that the particles migrate to a region shown by a dotted circle of radius given by R=0.38, where the non-dimensionalization of distances is done based on the shortest side of the channel cross-section, from the center of the square duct (figure 8(a)). The final particle positions are found to be at an average distance of 0.12 away from the wall, which is consistent with the observations of Chun and Ladd [35], who report the corners and region near the centers at a distance of 0.13 from the walls to be stable equilibrium positions. In figure 8(b), the particle trajectories for Re=100 are shown. It can be observed that the particles near the walls are 'repelled' away from it, due to a lubrication force that is generated because of the viscous forces generated in the thin film sandwiched between the particles and the wall. On the other hand, particles close to the center have a constant outward movement directed away from the center of the channel.

This inward movement can be explained based on the curvature of the velocity profile, which changes rather smoothly near the center and is sharp away from the center.

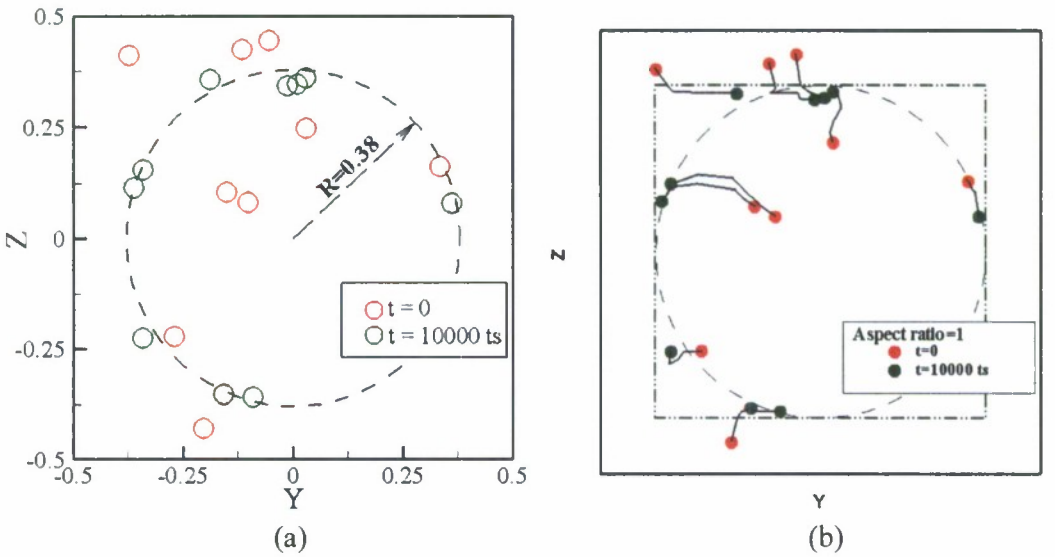

Figure 8: Final equilibrium positions at 10,000ts for Re=100 and aspect ratio 1 channel

Simulation of neutrally buoyant particles at Re=250 for the square cross-section channel gives a slightly different picture. Figure 9 shows such a case. Particles were observed to move to the corners or a region close to the center of the sides. As compared to Re=100 (figure 8), the particles were observed to be more localized at certain preferred zones in the channel. More so, particles were found to be aligned in chains along the direction of the flow. Figure 10 shows the three-dimensional view of the channel and the particle locations. Chains of particles were found to be formed at an average distance of 0.107 from the walls of the channel. This observation is qualitatively consistent with the simulation results of Chun and Ladd [35], who observed a similar behavior at Re=300. Their results show that the length of the stable region along the sides of the channel decreases as Re is increased from 300 to 500. For Re=500, particles were shown to form uneven spaced clusters, and reside near the corners of the square cross-sectioned channel.

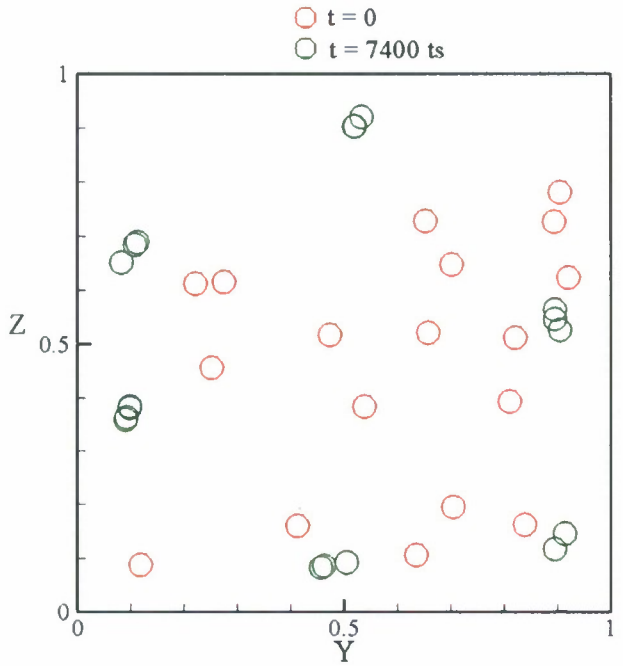

Figure 9: Equilibrium locations of particles at Re=250 and aspect ratio 1 channel

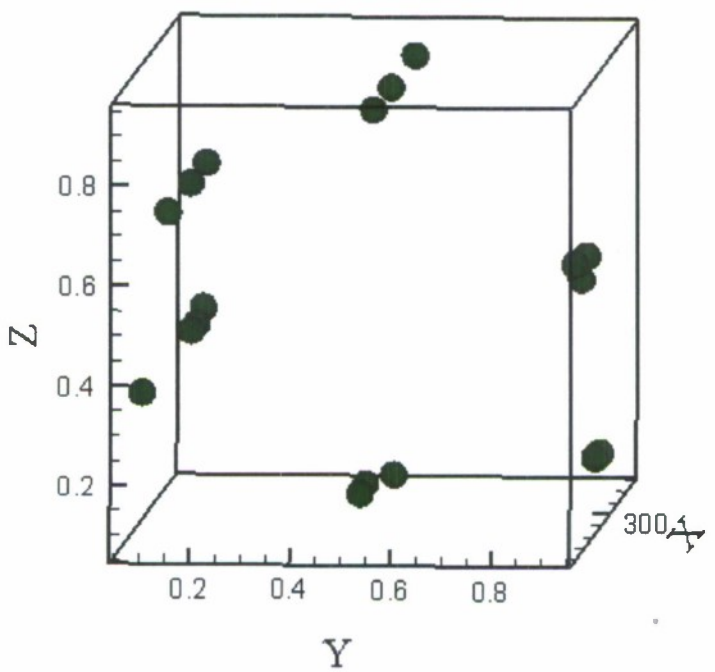

Figure 10: Formation of chains along the direction of the flow for aspect ratio 1 and Re=250

Results in microchannels of aspect ratio=2

Simulation results of inertial migration of neutrally buoyant spheres at an aspect ratio of 2 are described in this section. Sixteen particles of size d/H=1/10 were distributed randomly in the channel initially. Figure 11 represents the initial and final positions of these particles for Re=100 and compares these positions once equilibrium is reached. It can be observed that the particles tend to be spread over the shorter and longer sides of the channel, and are not localized to a certain point or region. The particles align along the longer side at an average distance of (0.176) from the wall. Along the shorter side, the particles were observed to be positioned at an average distance of (0.171) from the wall. Compared with the equilibrium locations obtained for a square cross-sectioned channel for Re=100, it is apparent that the particles are pushed farther away from the wall as the aspect ratio is increased.

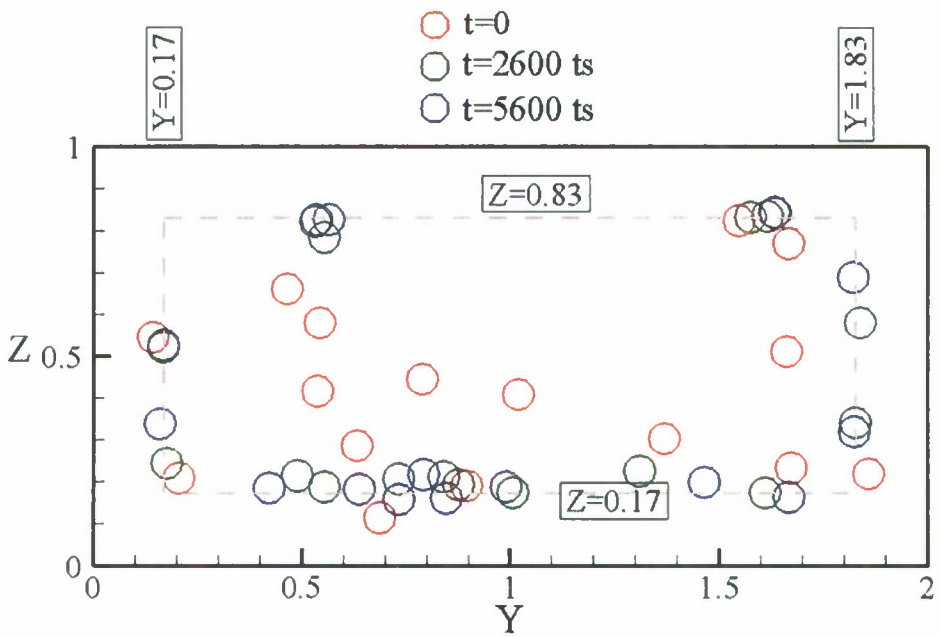

Figure 11: Particle locations for Re=100 and aspect ratio 2

Simulation results for a slightly higher Reynolds number of 250 show a slightly different trend. The migration is faster as compared to Re=100, as the particles experience a higher fluid inertia, which causes them to move faster in the lateral direction. Also, the number

density of particles near the corners of the channels is found to increase as compared to the former case. Moreover, particles tend to move away from the longer side of the channel. This indicates the presence of an inner ring, as shown in figure 12, which becomes apparent for the first time. In a recent experimental study [36], the presence of an inner ring of particles for a circular channel was reported for Re>600 for D/d=9-17. In figure 12, it can be observed that the particles migrate to two equilibrium positions, given by 0.14 and 0.25 from the walls at 5600ts. The outer ring moves more close to the wall for Re=250 as compared to Re=100, consistent with the arguments laid by the perturbation theories.

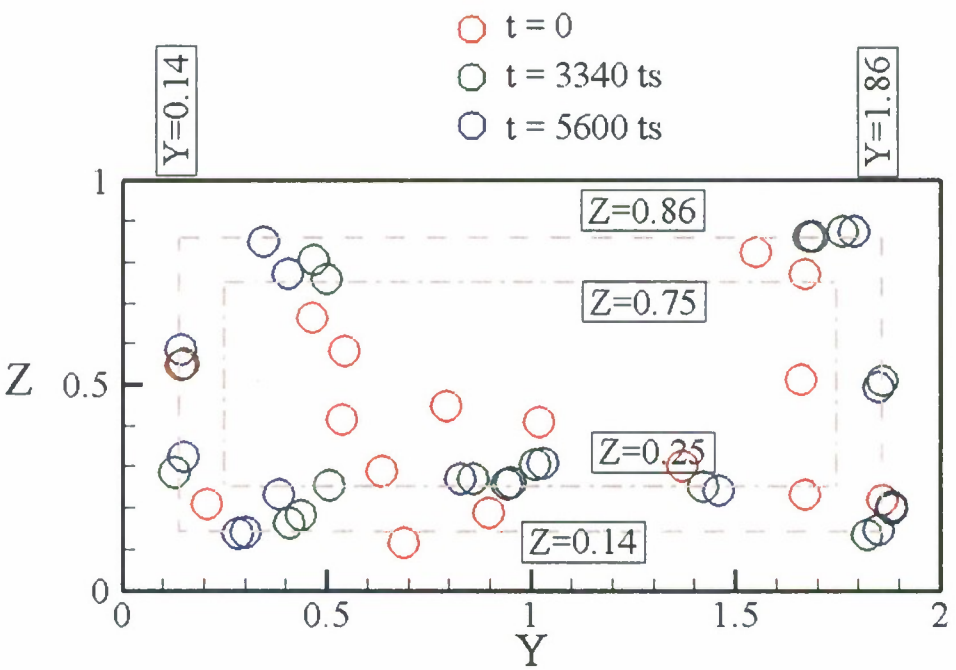

Figure 12: Particle locations for Re=250 and aspect ratio 2

As the Reynolds number is increased further, it was observed that the region around the centers of the longer faces is depleted of any particles (see figure 13). Instead these particles move inwards towards the center of the channel, thereby pushing the inner ring farther away from the walls. The outer ring of particles is found to be at a distance of 0.27 from the wall. On the other hand, particles near the vertical walls tend to move outwards

and ultimately reside at a location of 0.1 from the walls. The particle concentration was also found to be increase near the corners.

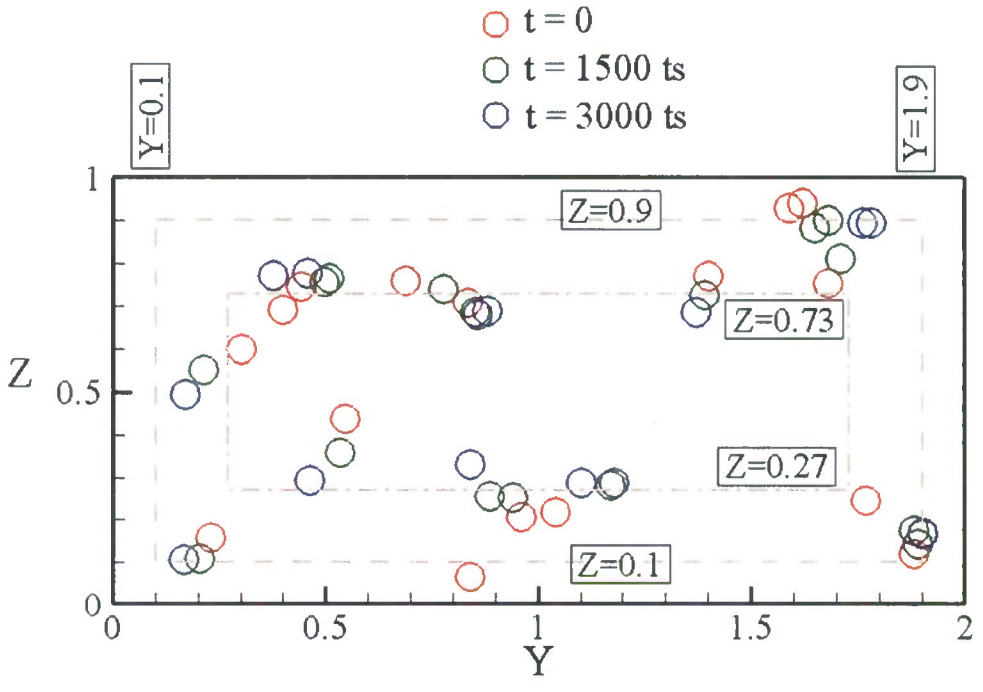

Figure 13: Particle locations for Re=500 and aspect ratio of 2

Results in microchannels of aspect ratio = 4

Simulation results of inertial migration of neutrally buoyant spheres in a channel of aspect ratio 4 are described in this section. Similar to Re=250, 16 particles of size d/H=1/10 were distributed randomly in the channel initially. Different pressure gradients were employed to drive the Poiseuille flow. Figure 14 represents the migration pattern of these neutrally buoyant particles for Re=100. As can be observed, particles near the walls are pushed inwards and particles near the center move outwards. At equilibrium, particles were found to reside at a distance of 0.2 from the walls. This distance is more as compared to the same inertia case for aspect ratio of 2, where the particles were found to be at a distance of 0.17, indicating the role of wall forces exerted from the longer dimension.

At a slightly higher Reynolds number of 250, a behavior similar to the same Re case of A=2 is observed (see figure 15). Particles were found to be repelled away from the longer side wall. A fraction of the particles were observed to migrate to positions that were 0.13 away from the walls, forming an outer ring. The rest of the particles reside at a distance of 0.27 from the walls. A quantitative comparison of the same case for A=2 reveals that both the inner and outer rings are not at the same locations for the two different aspect ratio cases. For A=2, the outer (inner) ring was found to be at a distance 0.14 (0.25) from the walls, whereas for A=4, this distance was calculated to be 0.13 (0.27).

To compare this shifting of the inner and outer rings with change in Re and aspect ratio, results of a simulation conducted for Re=500 is shown in figure 16. For this flow, the number density of particles in the inner ring is higher than the number density of particles that migrate to the walls of the channel. The presence of an inner and outer ring is also clear, with these regions located at a distance of 0.3 and 0.1 from the walls respectively.

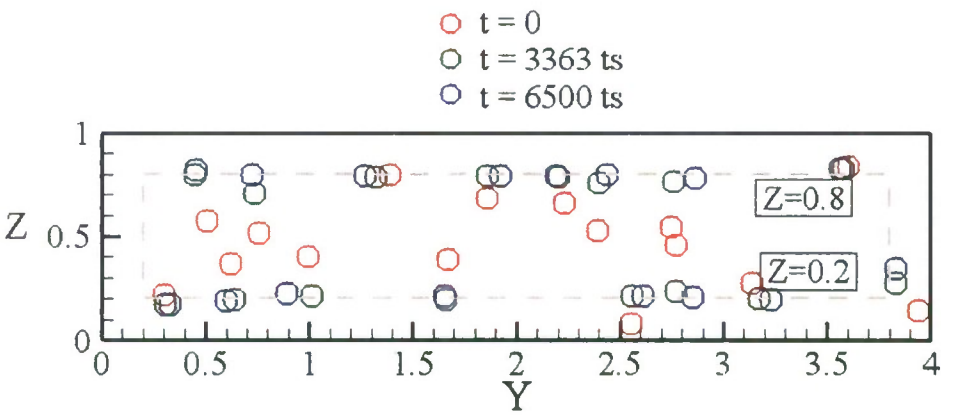

Figure 14: Particle positions at different time instants for Re=100 and aspect ratio of 4.

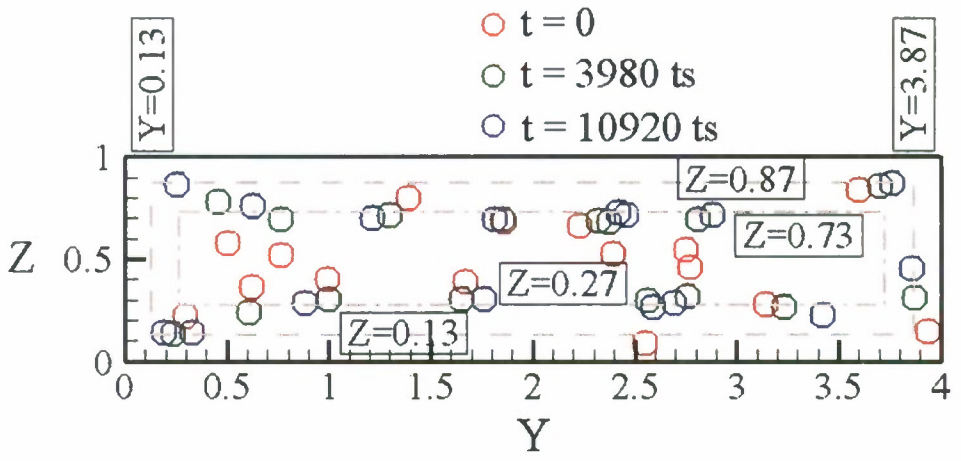

Figure 15: Particle positions for Re=250 and aspect ratio of 4

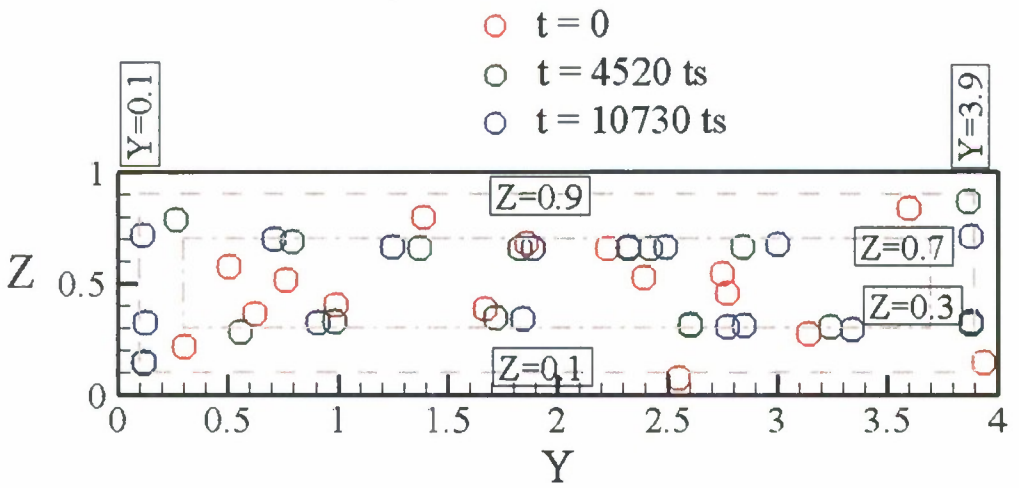

Figure 16: Particle positions at different times for Re=500 and aspect ratio of 4 - The horizontal dotted lines indicate the equilibrium locations along which the particles seem to align, at 0.1 and 0.9 (outer ring) and 0.3 and 0.7 (inner ring)

Experiments have revealed that as Re is increased, the probability of finding a particle in the inner ring is higher as compared to the outer ring [36]. More so, for D/d=42, the presence of the inner ring was not observed until Re>1200, and the inner ring was found to be centered at a distance of about half of the radius from the center of the circular channel. Current simulation results indicate a similar behavior for H/d=10. For Re=500 and A=4, the inner ring is found to be located at a distance of 0.3 from the walls (0.2 from the center). In addition, the number of particles that migrate to the inner ring is more

than twice the number of particles in the outer ring. With an increase in inertia of the flow, the inner ring is found to move towards the center of the channel between Re=250 and Re=500.

Asymptotic theory predicts that for planar Poiseuille flows, the particles move to a location that is 0.12, 0.09 and 0.08 far from the walls for Re=100, 250 and 500 respectively. Table 1 summarizes the results obtained using LBM simulations for different aspect ratios with the theoretical analysis for planar Poiseuille flow [37]. To summarize, particle migration locations are dependent on the aspect ratio and the inertia of the flow. As the Reynolds number is increased, the particles move to an equilibrium location that is closer to the wall. On the other hand, as the aspect ratio is increased, the relative equilibrium distances from the wall increase as well. For Re>250 for both aspect ratios of 2 and 4, an inner ring of particles was formed. The location of this inner ring is also a function of the Reynolds number and the aspect ratio. With an increase in either of the two, the ring was observed to shift to a location that was farther away from the wall.

Table 1: Particle equilibrium locations for different Re and aspect ratios. The values of the inner rings are mentioned in brackets.

Re	A=1	A=2	A=4	Theoretical Solution [37]
100	0.12	0.17	0.2	0.12
250	0.107	0.14 (0.25)	0.13 (0.27)	0.09
500	-----	0.1 (0.27)	0.1 (0.3)	0.08

3.2c Conclusion

In this work, inertial migration of neutrally buoyant particles in three-dimensional rectangular channels has been simulated using LBM. Simulation results were presented for cross-section aspect ratios of 1, 2 and 4, for 100<Re<500 with the channel to particle size ratio fixed at 10, and compared with existing experimental data [19, 36] asymptotic theory [38], and simulation results for a square channel [35]. Migration was found to be faster in the first half of the total migration time. During this time, the particles seem to cut the flow streamlines, whereas in the second half these particles move parallel to the

walls until they reach a final equilibrium position. For aspect ratios higher than 1, a difference in the migration location was observed. For a fixed Reynolds number, the distance of the equilibrium positions from the walls was found to be increase as the channel aspect ratio was increased. For Re=100, all the particles were found to migrate to an outer ring. The separation between this particle rich zone and the wall was found to be larger as compared to those for A=1. For Reynolds number above 250, the presence of an inner ring was evident, whose distance from the wall is found to increase with increasing aspect ratio. For a fixed aspect ratio and Re>250, the particles in the inner ring were found to be pushed further away from the wall as the flow Reynolds number was increased. The presence of the inner ring has previously been discussed for circular and square cross-sectioned channels, and was reported to appear for Re>500 with H/d=10. Current simulation results indicate that the presence of an inner ring is possible for channels with A>1 and Re>250.

3.3. Particle Simulation using DFM

As mentioned in previous section, the maximum concentration of particles that was used in LBM was less than 0.5%. For simulations using LBM the maximum number of elements used for simulation is just a few. Even though lattice Boltzmann methods can provide valuable insight to many body interactions, solutions could theoretically be found for each particle, but due to the multibody interactions the mathematics becomes complicated with even just a few. The number of particles explicitly modeled in these simulations is currently limited to the order of several thousand using high-end computers because of the large CPU and memory requirements.

The particle migration also depends on particle concentration and presence of more number of particles will help in increasing the heat capacity of the fluid during melting. For higher concentrations, DFM was used to solve the particle distributions and the results were used for analyzing the thermal performance of slurry. This model was introduced and described in the last year annual report and the results obtained this year by using this model are presented.

3.3a Diffusive Flux Model

For particle suspensions with large number of particles, it is reasonable to consider the suspension as a continuum for most applications because many suspended particles are less than a few micrometers in diameter. From a practical point of view, a macroscopic constitutive equation is preferable, as it allows the modeling of realistic macroscopic problems that contain extremely large number of suspended particles. Several constitutive models have been put forth recently which fall into two categories. One category comprises of models based on conservation of mass and momentum for suspension components [20], the other category comprises models based on shear-induced particle migration and diffusion [26].

The second category models, collectively referred as diffusive flux model (DFM) are based on the scaling arguments proposed in [24]. Leighton and Acrivos [37] suggested phenomenological models for particle migration in nonhomogeneous shear flow typically due to spatial variation in irreversible interaction frequency and effective viscosity. Phillips et al. [26] adapted the scaling arguments of Leighton and Acrivos, and proposed a diffusive-flux equation to describe the time evolution of the particle concentration based on the two-body interactions.

For analyzing the particle distribution effect on thermal performance for high concentrations, the Diffusive Flux model (DFM) proposed by Philips et al. [26] was used.

This method as applied to a three-dimensional rectangular duct can be summarized as follows. The shear-induced migration of particles is the result of shear rate gradients and the concentration gradients. The particle flux based on the phenomenological model is given by:

$$J = -K_c a^2 \phi \nabla(\phi \dot{\gamma}) - K_\eta a^2 \frac{\phi^2}{\eta} \nabla \eta \tag{7}$$

K_c and K_η are the phenomenological constants that must be determined by fitting the predictions of the model and the experimental results. These values for both 2-D tube and channels flows were predicted as 0.62 and 0.41. The dynamics change of particle concentration along the flow is governed by the particle balance:

$$\frac{D\phi}{Dt} = \nabla . J \tag{8}$$

With the assumptions mentioned above, the mass and momentum equations for the phase change slurry can be written as:

$$\nabla . \vec{u} = 0 \tag{9}$$

$$\nabla . \left[\eta(\nabla \vec{u} + \nabla \vec{u}^t)\right] - \nabla p = 0 \tag{10}$$

The effective viscosity is of a concentrated suspension can be given by the Krieger's formula [27]:

$$\eta = \eta_f \left(1 - \frac{\phi}{\phi_m}\right)^{-m} \tag{11}$$

where the maximum concentration can be 0.6 to 0.68 and the empirical m is equal to 1.82. Diffusive flux model is valid for slow flows and it can be used for particle Reynolds numbers less than 0.1 [28]. K_c and K_η are the phenomenological constants that must be determined by fitting the predictions of the model and the experimental results.

Boundary conditions for flow and particle distribution

For particle distribution, the following boundary conditions are used

$\phi = \phi_0$, at the inlet (12)

$[\eta(\nabla u + \nabla u^T)]n = 0 \quad p = p_0$, particle outlet (13)

$n.[K_c \phi \nabla(\dot{\gamma}\phi) + K_\eta(\dot{\gamma}\phi^2)\frac{1}{\eta}\frac{\partial \eta}{\partial \phi}\nabla\phi] = 0$, the total flux at the wall and the symmetric boundary is zero. (14)

Developing length of particle distribution

Particle distribution can be considered to achieve the equilibrium position if there is no change in the particle profile. Nott and Brady [20], analyzed the time scale for particles to reach steady state based on the shear-induced-diffusion hypothesis [39] and is given by:

$$t_{ss} \sim \left(\frac{2W}{a}\right)^3 \frac{a}{12d(\phi) < u >} \tag{15}$$

where W is half of the channel width, a is the particle radius, <u> is the average velocity. For dense suspensions, (φ>0.3), 12d(φ)~1. Hence the length along the channel required to achieve steady state is given by:

$$\frac{L_{ss}}{2W} \sim \frac{1}{12d(\phi)}\left(\frac{2W}{a}\right)^2 \tag{16}$$

This length is the characteristic length scale for the process and it requires several transition lengths before the final equilibrium state is reached. Experiments by Hampton et al. [29] shows a range of values for the exponent n, increasing linearly from 0.4 for φ = 0.2 to 1.8 for φ = 0.45. Authors in [30] found that the value of n is around 1 for particle concentration of 0.24 and around 2 for particle concentration of 0.35. Assuming H = 100 μm, a = 2.5 μm and particle concentration is 0.3, which is between 0.24 and 0.35, particle steady state profile can be achieved between a length of 4 cm and 16 cm. It can be observed the migration development length is very long compared to the usual length of MMC heat sinks, which is around 1mm. Hence, the effect of particle migration on thermal performance was investigated in traditional microchannel heat sinks.

For the present study, the particle distribution is modeled in microchannels of large aspect ratio (>=10), where the flow can be considered to be two-dimensional. This was done in order to use the readily available 2-D values for K_c and K_η. This is justifiable since the main aim of this work is to look at the thermal performance of nonhomogeneous slurry in a microchannel.

Assumptions for thermal simulation

For solving the temperature of slurry, the problem was formulated based on the following assumptions.

i. The slurry properties are a function of particle concentration. Segre and Silberberg [19] found that the radial migration of the particles is a function of 2.84^{th} power of particle/duct diameter ratio. When the duct or channel size is very small like in the case of microchannel, the ratio can be large.

ii. The specific heat capacity of the fluid is a function of temperature. The slurry thermal conductivity is a function of the particle Peclet number and varies across the flow field.

iii. The melting inside EPCM particles takes place over a range of temperatures, between T_1 and T_2 with the peak melting point at a temperature, T_m.

iv. There is no temperature gradient inside the particle or the particle melts instantaneously. This assumption has been discussed in later sections. The particle sizes, where this assumption is valid will be considered for simulation

v. The effect of particle depletion layer is negligible. The particle depletion layer is of the order of the particle radius if the channel size to particle size is large [40, 41].

vi. The shape of the encapsulated particles is spherical. The shell material is very thin and hence the particles are considered to consist totally of the phase change material.

Validation of assumptions for thermal simulation

- Assumption iv: Particle melts instantaneously

Since the length of the channel is short for the MMC channel, it is important that the PCM particle completely melts within its residence time. Charunyakorn et al. [8] applied the method proposed by Tao [42] to calculate solid-liquid or melt interface r_p (Figure 17) in a sphere for calculating the source term in their model.

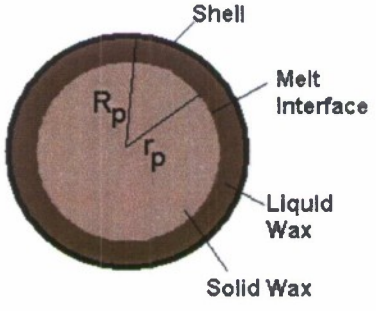

Figure 17: Particle melting process

Assuming the particle has to melt 99% by the time it exits the channel, the required temperature difference between the surrounding fluid T_f and the melting temperature T_m, of the PCM was calculated (Equation 17) using the same analogy.

$$T_{fm} = T_f - T_m = \left[\frac{1}{2}\left[1-\left(\frac{r_p}{R_p}\right)^2\right]+\frac{1}{3}\left[1-\left(\frac{r_p}{R_p}\right)^3\right]\left(\frac{1}{Bi_p}-1\right)\right].\frac{h_{sf}.R_p^{\,2}}{t.\alpha_p.c_p} \tag{17}$$

Where the Biot number of the particle is given by:

$$Bi_p = \frac{k_{eff}}{k_{pcm}}.\frac{2(1-c)}{2-3c^{\frac{1}{3}}+c} \tag{18}$$

Figures 18 and 19 show the required temperature difference between the fluid and the particle melting temperature with water and PAO as base fluids in a channel of 100 μm width and 1 cm length for different Re. It can be observed that the required T_{fm} increases with the increase in particle radius. It can be observed that the particle may not be completely melted if the channel length is short. For calculations properties in Table 2 were used.

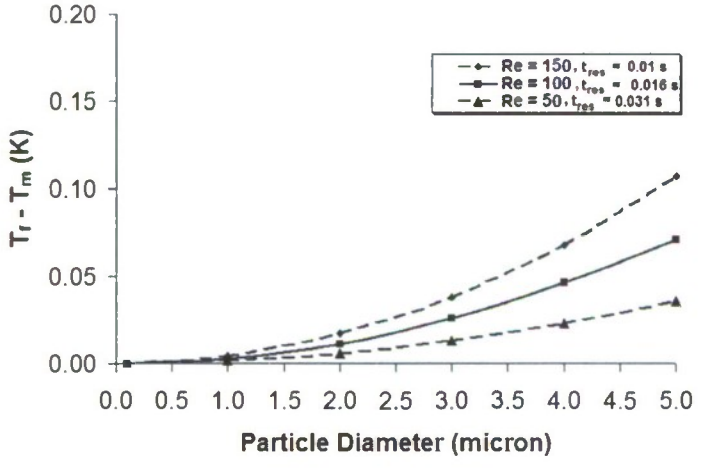

Figure 18: $T_f - T_m$ for different particle diameters (base fluid - water)

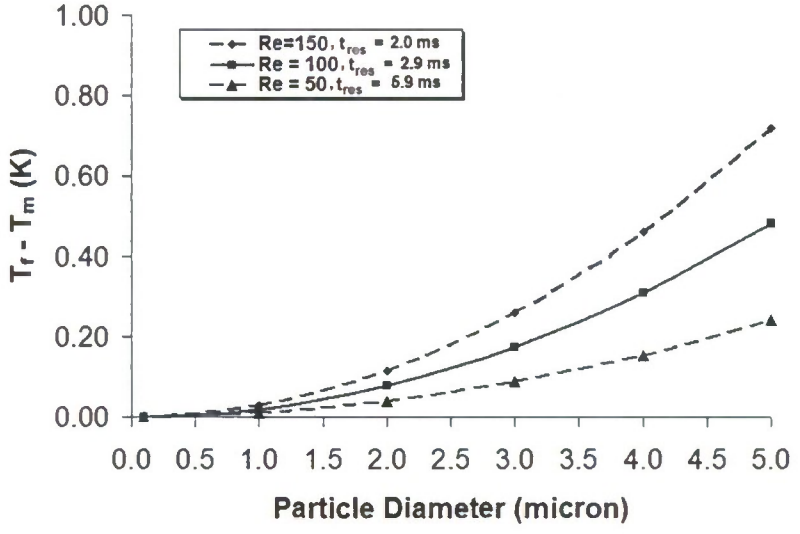

Figure 19: $T_f - T_m$ for different particle diameters (base fluid - PAO)

Table 2: Thermophysical properties used in Figures 3.2 and 3.3

	Density (kg/m^3)	Specific heat (J/kg.K)	Thermal conductivity (W/m.K)	Viscosity (kg/m.s)	Latent heat (J/kg)
PAO	783	2242	0.143	4.45×10^{-3}	-
n-octadecane	815	2000	0.18	-	244×10^3
Water	997	4180	0.604	1×10^{-3}	-

Governing equations for thermal simulations

After the particle distribution is solved using the DFM, the thermal performance of slurry will be modeled assuming slurry as a bulk fluid with varying properties which are a function of particle concentration. The energy equation for the slurry and the boundary conditions are:

$$\rho c_p \left(u\frac{\partial T}{\partial x} + v\frac{\partial T}{\partial y} \right) = \frac{\partial}{\partial x}\left(k\frac{\partial T}{\partial x} \right) + \frac{\partial}{\partial y}\left(k\frac{\partial T}{\partial y} \right) \tag{19}$$

$T = T_{in}$ at the inlet for fluid (20)

$q.n = (\rho c_p \mathbf{u} T).n$; convective heat flux boundary condition at the outlet/exit (21)

$q.n = q_w$; constant heat flux at the wall (22)

$q.n = 0$; insulation at the symmetry or channel half-width (23)

Effective Thermal Conductivity

Slurry thermal conductivity and specific heat is defined follows. For dilute suspensions of static bulk fluids, thermal conductivity of the suspension can be defined as for conductivity in a medium with distributed spherical particles [12]:

$$k_b = k_f . \frac{2 + \frac{k_p}{k_f} + 2c(\frac{k_p}{k_f} - 1)}{2 + \frac{k_p}{k_f} - c(\frac{k_p}{k_f} - 1)} \tag{24}$$

Yamada and Takahashi [43] investigated experimentally the thermal conductivity of suspensions of particles of different shapes. They found an excellent agreement between their experimental values for suspensions of spherical particles. The results for other shapes compare less favorably. For flowing slurries, the effective thermal conductivity is higher than that calculated by Equation 3.18 due to diffusion related enhancements. For dilute suspensions, it can be evaluated as follows [8]:

$$k_{eff} = f.k_b \tag{25}$$

$$\begin{cases} f = 1 + BcPe_p^m \\ B = 0, \quad m = 1.5, \quad Pe_p < 0.67 \\ B = 1.8 \quad m = 0.18 \quad 0.67 \le Pe_p \le 250 \\ B = 3.0, \quad m = \frac{1}{11}, \quad Pe_p > 250 \end{cases}$$

The particle Peclet number is defined as,

$$Pe_p = \frac{ed_p^{\,2}}{\alpha_f} \tag{26}$$

Since the velocity is not fully developed in the current analysis, the shear rate is a function of all the spatial coordinates and corresponding velocities. The magnitude of the shear rate, e can be calculated using the following equation:

$$e = \left(\frac{1}{2} \sum_i \sum_j \gamma_{ij} \gamma_{ji} \right)^{1/2} \tag{27}$$

γ is the shear rate.

Effective Density

For slurries, the density can be calculated by the weighted mean method given below [8]:

$$\rho_b = c\rho_m + (1-c)\rho_f \tag{28}$$

The mean density, ρ_m is the average of the densities of PCM solid and liquid phases.

Effective Specific Heat

The phase change inside the particles can be modeled using latent heat method or effective specific heat capacity method. Latent heat method can be used to model pure PCMs where as the effective specific heat method can model the melting range of PCMs easily. Alisetti and Roy [44] have used various profiles for the specific heat of PCM for calculating the effective specific heat and have shown that the difference between the solutions is less than 4%. When PCMs are encapsulated, due to the nucleation, there usually is a melting range for the PCMs, and this increases with decrease in particle size. Of all the different profiles, sine profile (Figure 20) has been used to represent EPCM particle specific heat. This was done in order to avoid sudden variation in the property and help in having less convergence problems. As there is not much variation, the specific heat of solid and liquid phases of PCM is assumed to be equal.

$$c_{p,p} = c_{p,pcm} + \left\{ \frac{\pi}{2} \left(\frac{h_{sf}}{T_{Mr}} - c_{p,pcm} \right) . \sin \pi \left[\frac{(T - T_1)}{T_{Mr}} \right] \right\} \tag{29}$$

The effective specific heat of the slurry can be calculated as:

$$c_{p,b} = c_m c_{p,p} + (1 - c_m) c_{p,f} \tag{30}$$

The value specific heat of the particle in Equation 30 is equal to $c_{p,pcm}$ when the temperature of the particle is outside the melting range and is given by Equation 29, when the particle temperature is within the melting range.

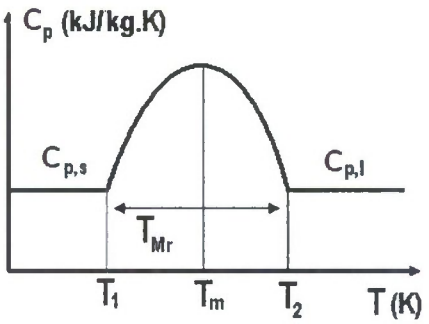

Figure 20: Specific heat of EPCM, function of temperature

3.3b Particle Distribution Results

The microchannel dimensions used for simulation of particle distribution are 100 μm width, 1mm height and 1 cm length. As mentioned before, the simulation domain can be considered 2D for such high aspect ratios. Commercial software COMSOL was used for all the numerical simulations in the work [45]. Following parameters were varied.

i. Base fluid: Two different fluids were used, water and poly-alpha-olefin (PAO). PAO is a dielectric fluid used for cooling of military avionics applications. It is a stable and inexpensive fluid.

ii. Particle diameter: 100nm, 1 μm, 5 μm

iii. Particle concentration: 0.05, 0.1, 0.3

iv. Channel Reynolds number: Since DFM is valid for $Re_p <= 0.1$, it was found that the maximum Reynolds number of the fluid that can be modeled was calculated using the following calculation:

$$Re_p = Re_{max}(a/H)^2 \quad (31)$$

For current simulation, a = 2.5 μm, H = 100 μm. Substituting the value of Re_p = 0.1, Re_{max} is 160. Thus three different channel average Reynolds numbers were used for simulating the particle migration. Table 3 below shows the inlet velocities when water and PAO were used. For the calculations, the density and viscosity of pure fluid are used from Table 2.

Table 3: Re values used for simulating particle migration

Channel Re_{avg}	$V_{in,\ Water}$	$V_{in,\ PAO}$
80	0.357 m/s	2.276 m/s
60	0.268 m/s	1.707 m/s
30	0.134 m/s	0.85 m/s

Effect particle diameter on particle migration

Figure 21 shows the particle distribution at a length of 1 cm for all the three particle diameters used with PAO as base fluid. The particle mass concentration is 0.3 and Re_{avg} is 80. It can be observed that the migration is highest for 5 μm particle and there is no migration for 100 nm particle size.

Effect of particle volume concentration on particle migration

Figure 22 shows the particle migration at a length of 1 cm from the inlet for a particle diameter of 5 μm and Re_{avg} of 80. It can be observed that the migration is high when the particle mass concentration is higher.

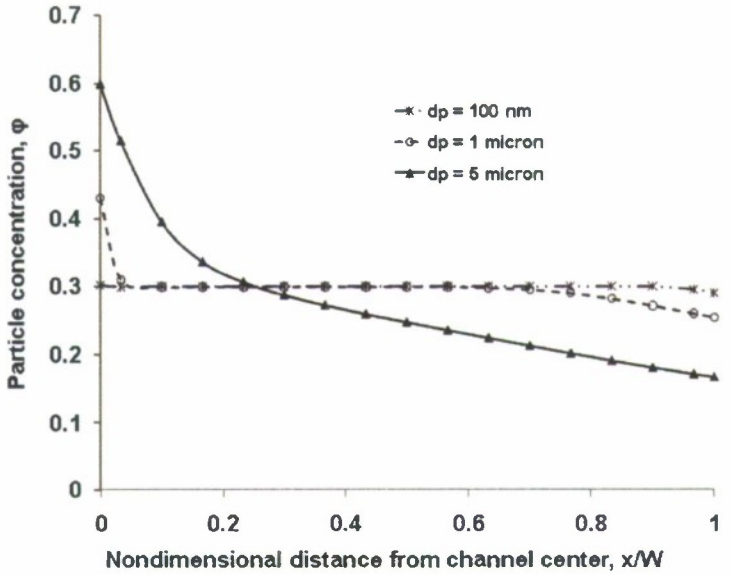

Figure 21: Particle distribution with varying particle diameter (PAO)

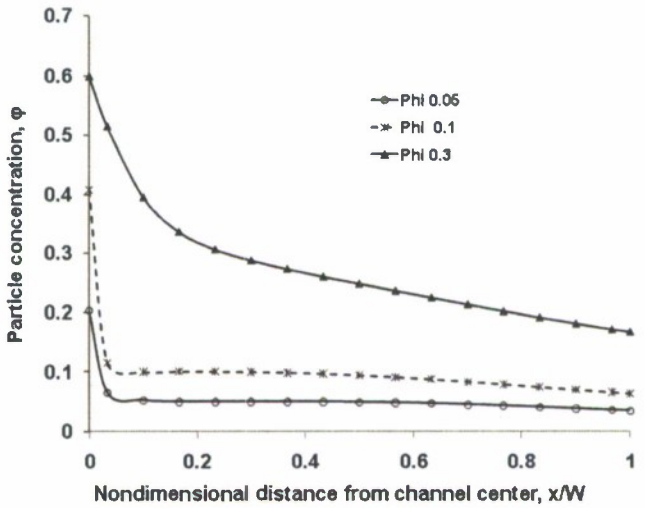

Figure 22: Particle distribution as a function of concentration (PAO)

Effect of inlet velocity on particle migration

Simulations with three different Re_{avg} were run and it was found that there was no effect of inlet velocity on particle migration. Figure 23 shows the particle concentration profile obtained with water based slurry for all three Re_{avg}. This type of result was also obtained

in [46]. The reason could be that the diffusive flux model does not include the inertial forces and hence the variation in velocity does not effect the particle migration. The variation in concentration profile was only dependent on the a/H ratio, i.e., the particle radius to the tube radius or channel width.

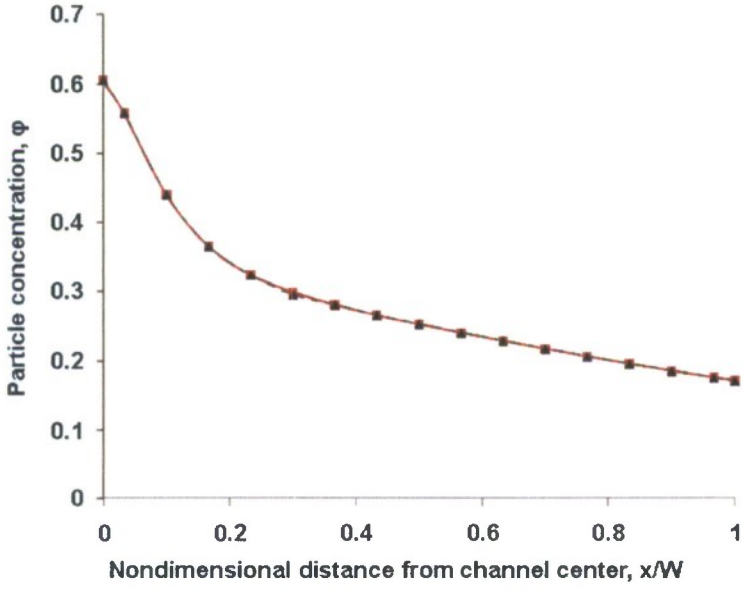

Figure 23: Particle distribution profile (base fluid – water)

Particle migration along the length of the channel

It is interesting to observe the transformation of homogeneous profile into nonhomogeneous along the length of the channel. Figure 24 shows the particle distributions at different lengths from inlet for PAO. The Re_{avg} used is 80 and particle concentration is 0.3. It can be observed that the particle migration rate increases with increase in length.

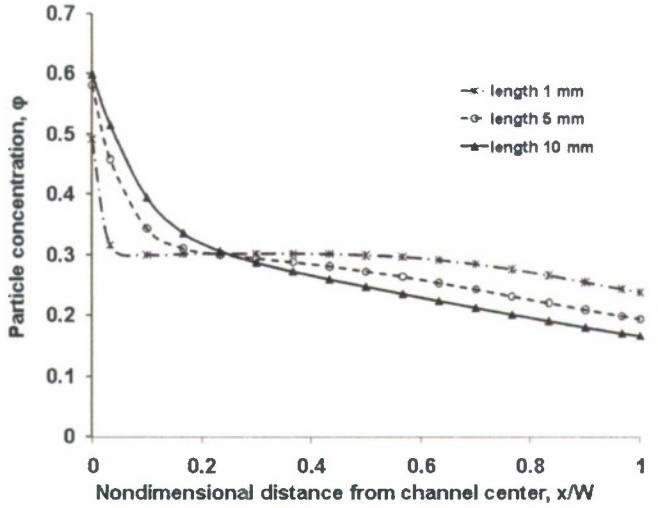

Figure 24: Particle concentration at different locations along length (PAO)

3.3c Thermal Performance Results

The effect of particle migration on thermal performance was investigated by comparing the thermal results obtained assuming the particle profile is developing (uniform profile at inlet and nonuniform profile at the exit as shown in Figure 25) and the results obtained assuming the particle profile is homogenous (uniform at both inlet and exit as shown in Figure 26).

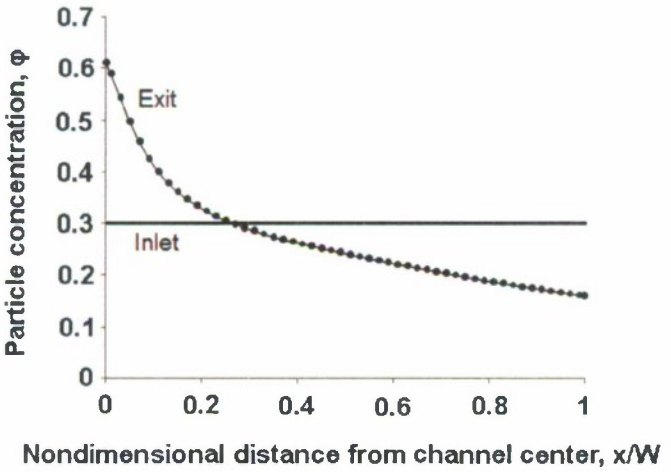

Figure 25: Particle concentration profile for developing assumption

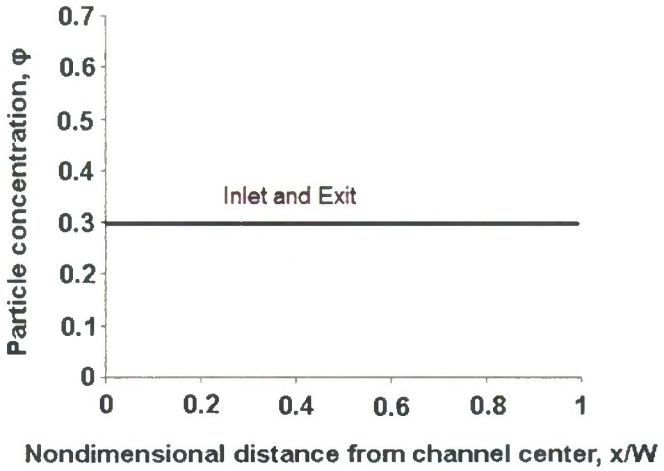

Figure 26: Particle concentration profile for homogeneous assumption

The particle distribution obtained for a particle diameter of 5 μm and particle concentration of 0.3 was used for thermal simulations as maximum migration was observed at these conditions. Figures 27 and 28 show the difference in maximum wall temperature and the inlet temperature for both fluids. The average Re used was 80 and a melting range of 6 K was used. PCM melting peak was assumed to be at 27 ^{0}C. The difference in wall temperature for both assumptions is not more than 1.4 K for water and is 1 K for PAO.

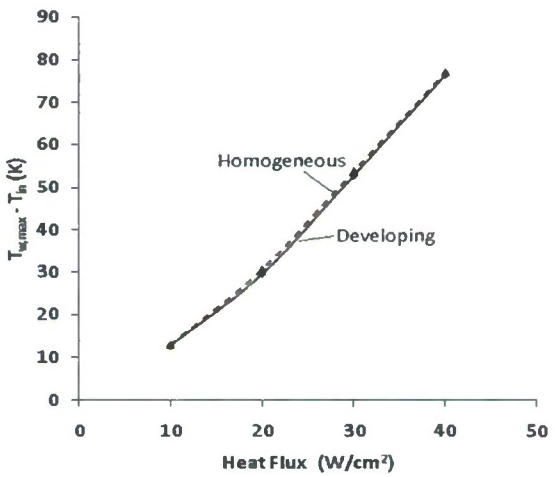

Figure 27: Difference in maximum wall temperature and inlet temperature for both assumptions (fluid – water)

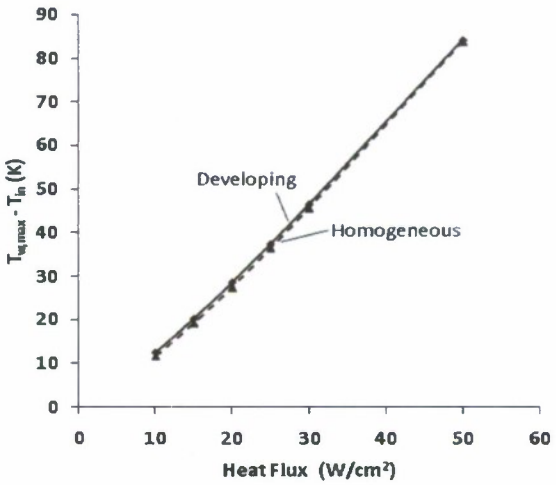

Figure 28: Difference in maximum wall temperature and inlet temperature for both assumptions (fluid – PAO)

Analysis of the results

From previous results, it can be understood that the maximum wall temperature difference for both particle distribution assumptions was not more than 1.4 K for all the heat fluxes considered. The reason can be:

- *Simultaneous developing of both concentration and temperature profiles*

Since the concentration profile is still developing along the length, the deviation of concentration from the average value (0.3) is not immediate. Figure 29 shows the concentration profile at a distance of 35 μm from the center (x/W = 0.7) along the length of the channel from inlet for PAO. It can be observed that the minimum value of particle concentration at the wall is 0.23, which happens to be at the exit. Figure 30 shows the resultant local wall temperature from inlet to exit, assuming both homogeneous and developing particle distributions. It can be observed that the local wall temperature for both cases is same up to a certain length of the channel. The difference in temperature profiles for both cases will be the combined effect of thermal boundary layer and particle distribution development, which is negligible for a certain length of the channel. It should

also be noted that, once the local temperature is higher than the melting range, PCM latent heat is already used up and the effect of migration does not possibly affect the wall temperature. Hence, the difference between both assumptions did not affect the thermal performance considerably.

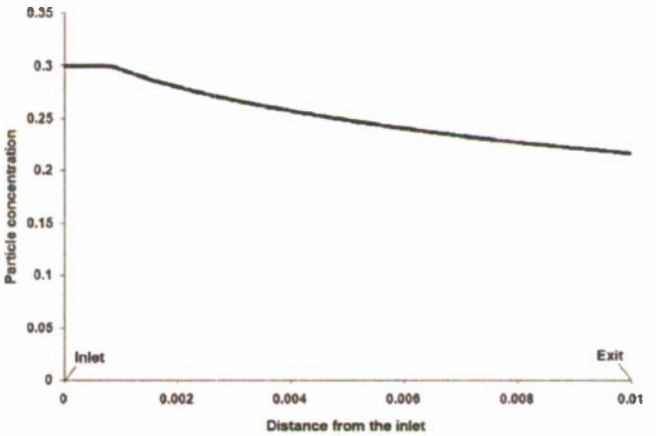

Figure 29: Particle concentration profile development along the channel

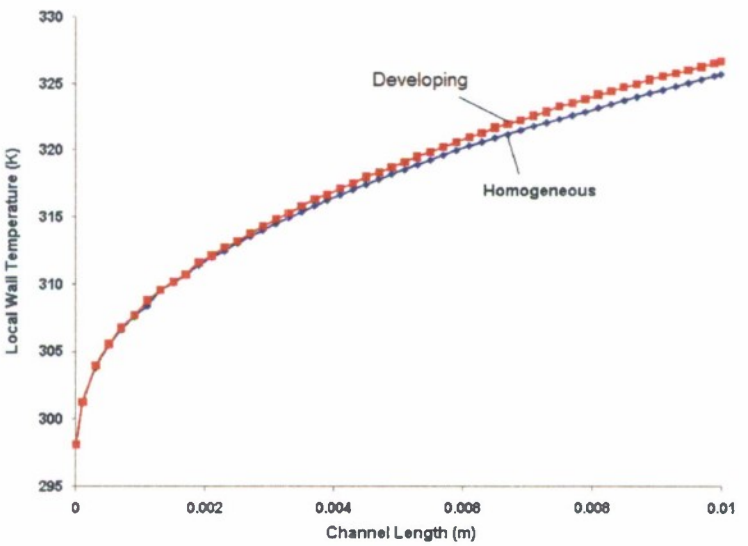

Figure 30: Local wall temperature for both profile assumptions along the channel

Another observation from the results is that the maximum wall temperature for developing profile assumption is lower compared to maximum wall temperature with homogeneous assumption in case of water. For PAO, this behavior was found to be opposite. The reason for this behavior can be the effective thermal conductivity of the fluid at the wall. In case of water, when homogeneous assumption was used, the thermal conductivity was lower at the wall resulting in less heat transfer from wall to fluid and hence high wall temperature compared to developing profile assumption. This behavior is reverse for PAO, i.e., the thermal conductivity is higher when homogenous assumption was used and hence lower wall temperature compared to developing profile assumption.

From the above analysis, it can be observed that the maximum error in predicting the wall temperature is around 1.4 K for the conditions used, if a homogeneous assumption is used instead of nonhomogeneous assumption. This value was obtained for water at a heat flux of 20 W/cm^2, and the value of $T_{wall} - T_{in}$ is 29.2 K for developing profile and 30.6 K for homogeneous profile. In practical applications, this small temperature difference can be neglected owing to the many assumptions used in numerical simulations. Unless very accurate prediction is needed, including the particle migration effect is not very crucial.

3.3d Thermal Performance with Fully Developed Profile Assumption

Since a major difference was not observed in developing and homogeneous profiles, another set of simulations were run to compare the thermal performance of slurry when the particle distribution is assumed homogeneous and the particle distribution is fully developed (Figure 31). Particle diameter used is 5 μm, particle concentration is 0.3 and Re_{max} is 160. Fluid used is PAO. For parametric study the effect of inlet temperature, base heat flux, melting range were studied. Figure 32 shows the concentration profiles at different lengths from inlet. From the figure, it can be observed that the particle migration rate reduces significantly after certain length from the inlet. The particle concentration profile varied rapidly from inlet up to 2.5 cm length and the change in concentration

profile variation from 2.5 cm to 10 cm is very slow. The difference between profiles at a length of 7.25 cm from inlet and 10 cm from inlet is negligible. Hence, it can be assumed that the particle profile is fully developed.

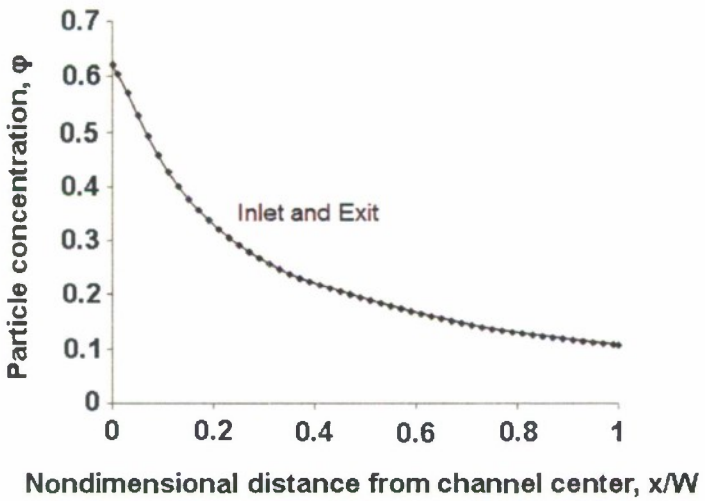

Figure 31: Particle concentration profile for fully developed assumption

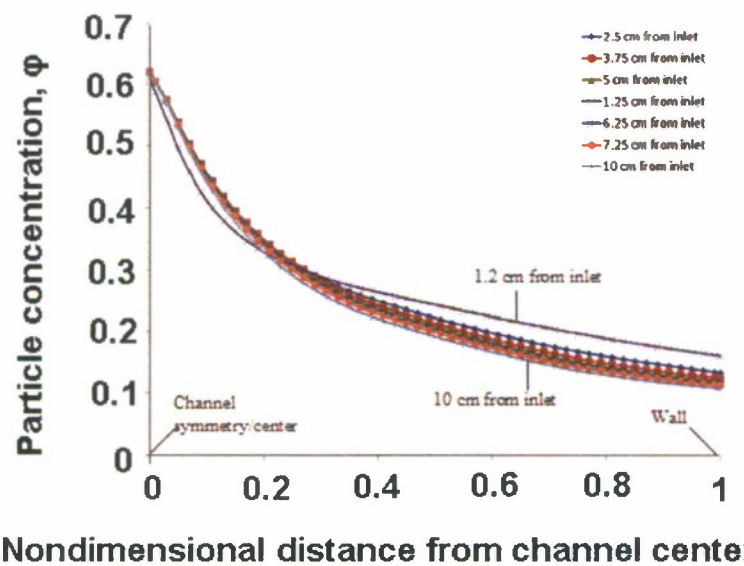

Figure 32: Particle concentration profiles at various lengths from inlet (base fluid - PAO)

Effect of fluid inlet temperature

The inlet temperature of the fluid was first varied at a heat flux of 20 W/cm^2 and melting range of 5 K (25.5 ^{0}C to 30.5 ^{0}C, and peak is 28 ^{0}C). Figure 33 shows the results. It can be observed that an inlet temperature of 26 ^{0}C (slightly after lower melting point) will be useful in obtaining the maximum thermal performance at any profile assumption. The wall temperature difference between homogeneous and fully developed profile assumptions is around 3.6 K, whereas the difference between homogeneous and developing profile assumptions is 1 K.

Effect of wall heat flux

Figure 34 shows difference between maximum wall temperature and inlet temperature for all the three assumptions. It can be observed that the wall temperature difference is maximum between fully developed and homogeneous assumptions is at a heat flux of 30 W/cm^2. When the heat flux is increased to 40 W/cm^2 and 50 W/cm^2, the bulk temperature of fluid at the outlet is near the melting end temperature (making the PCM specific heat compared to PAO) and hence the effect of migration decreases.

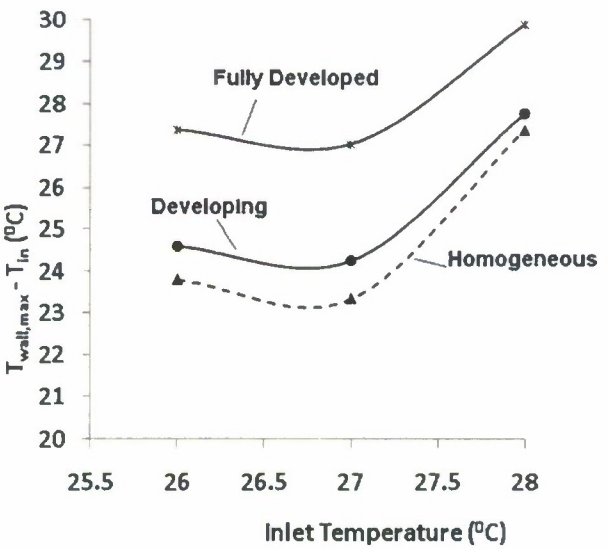

Figure 33: $T_{wall,\,max} - T_{in}$ vs. T_{in} for three assumptions at different inlet temperatures

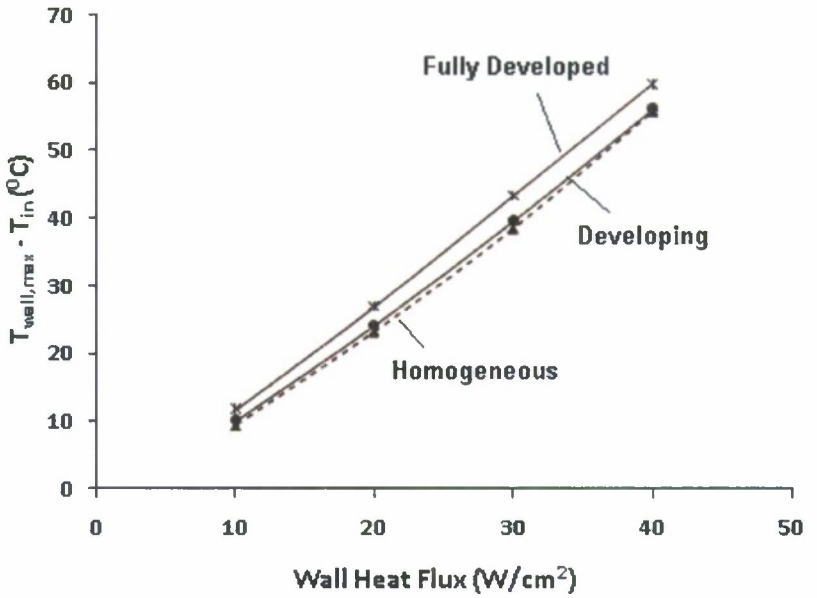

Figure 34: $T_{wall} - T_{in}$ for three profile assumptions at different heat fluxes

Effect of PCM melting range

Five different melting ranges were considered for the study. Figure 35 shows the result of varying melting range. It can be observed that thermal performance variation between homogeneous and nonhomogeneous assumptions decrease with increase in melting range. This can be due to lowered specific heat peak (because of averaging over a large melting range) which makes the latent heat effect of PCM comparable to specific heat of base fluid. Therefore, the effect of migration of PCM particles to center diminishes with increase in melting range.

Since a typical microchannel can also be 2 cm length, few more simulations were run to compare the thermal performance of slurry with developing profile and homogeneous profile. Figure 36 shows the comparison of wall temperature for both assumptions when the channel length is 2 cm. The maximum wall temperature difference between both profile assumptions was 1.2 K as compared to 1 K when the channel length was 1 cm.

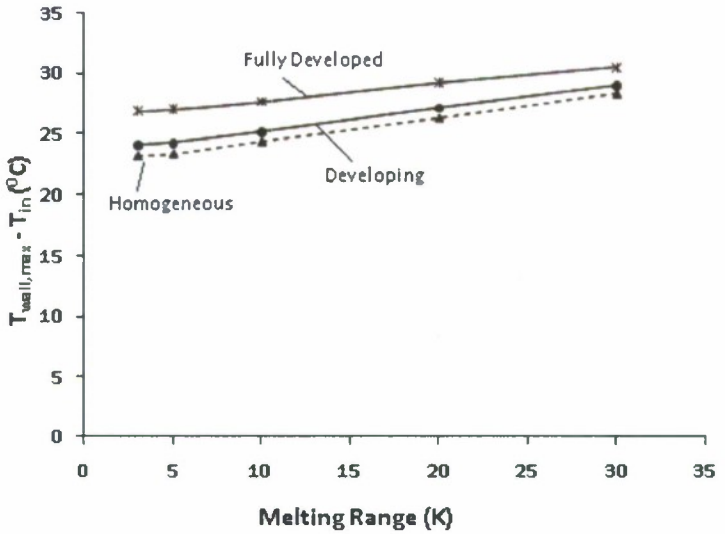

Figure 35: $T_{wall,\ max} - T_{in}$ for all three profiles at different melting ranges

The thermal performance of slurry was also analyzed in a 3D channel of 100 μm width, 1 mm height and 1 cm length. This was done to compare the maximum wall temperature obtained in 3D and 2D simulations. A base heat flux of 200 W/cm^2 (equal to 20 W/cm^2, at the wall for 2D) was used for 3D thermal simulations. Table 4 below shows the difference between 2D and 3D results for all the three assumptions. It was found that the maximum temperature of the wall (fluid-solid boundary in width direction) is slightly lower than the wall temperature predicted using 2D. This is because in case of 3D, the increase in wall heat transfer area because of the addition of the base results in a lower wall temperature.

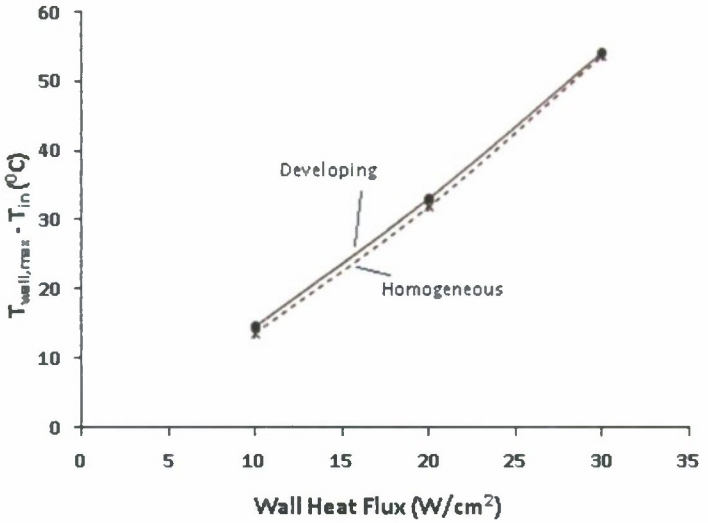

Figure 36: Results at a channel length of 2 cm

Table 4: Thermal results obtained in 3D using 2D particle distribution

Analysis	$T_{wall, HNT}$	$dT_{bulk, HNT}$	$T_{wall, NH}$	$dT_{bulk, NH}$	$T_{wall, H}$	$dT_{bulk, H}$
3D	322.34	300.9433	324.561	301.0379	322.031	300.8734
2D	323.409	299.9423	326.1888	300.121	322.491	299.9458

3.3e Conclusion

The migration was found to depend on the ratio of particle diameter to channel width. The larger the particle diameter, the more rapid is the particle migration. It was also found that the particle profile varied slightly when the base fluid is different. It was found that for very short lengths (~1 mm), the migration of particles is negligible.

Thermal simulations using the results of diffusive flux model showed that, when the profile is developing, the maximum wall temperature, $T_{wall,max}$ is around 1.4 K different compared to $T_{wall,max}$ obtained assuming homogeneous particle distribution. In case of water, the maximum wall temperature assuming developing profile is lower compared to the maximum wall temperature obtained assuming homogeneous distribution, where as

this behavior is opposite in case of PAO. The reason can be because of the decrease or increase in overall thermal conductivity of the fluid at wall. The maximum wall temperature in case of assuming fully developed profile showed a maximum difference of 5 K compared to that of assuming homogeneous distribution. However, for obtaining such profile, the length of channel should be very long or of the order of 10 cm in the case considered which is not likely in case of microchannels (due to the associated high pressure drops). Hence, it can be concluded that it is not important to include the particle migration in the numerical model.

3.4 Parametric Study in MMC Heat Sinks

The parametric study results presented last year comprises of investigating performance of PAO based slurry flow in MMC heat sinks. This section discusses the effect of base fluid thermal conductivity and channel dimensions on thermal performance of slurry. The model is briefly introduced here and parametric study results are presented after comparing with results obtained in heat transfer experiments. From section 3.3, it is evident that the particle migration effect is negligible and hence it is not included in the model.

3.4a Numerical Model

Schematic of the simulation domain

Figure 37 shows the schematic of the heat sink domain that was considered for parametric study. The flow rate at the entrance/inlet of the channel will be the total flow rate at the heat sink inlet divided by the total number of channels, assuming the same amount of flow rate enters each channel. Only half of the channel was considered for simulation due to symmetry.

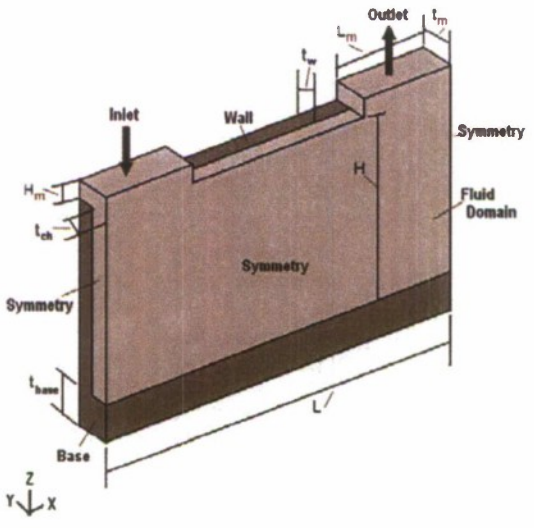

Figure 37: Schematic of flow domain

Dimensions used are shown in configuration – I of Table 5. It was assumed that there are 441 microchannels in the heat sink (the specifications of MMC heat sink used for heat transfer experiments) and the flow rate is assumed to be same at the inlet of each channel.

Table 5: Geometric configurations used for numerical simulation (units in μm)

Configuration	Base fluid	H	$2*t_{ch}$	L	H_m	$2*t_m$	L_m	$2*t_w$	t_{base}
I	Water, PAO	533	101	1000	50	201	250	352.52	250
II	Water	375	25	1000	100	100	250	75	250

Assumptions

All the assumptions mentioned in subsection 3.3 along with the following are used for formulating the problem.

i. The particle distribution is homogeneous. This is valid as explained in Chapter 3.

ii. Particle always follow the fluid

iii. The total volumetric flow at the inlet of heat sink is equally divided and is same in each channel.

Validation of assumptions major assumptions

- Assumption ii: Particle always follow the fluid

The amount of time taken by the particle to reach the fluid velocity can be calculated using Equation 32. Using the drag force on the particle (Figure 38)

$$F_D = m\frac{dv}{dt} = 6\pi\mu_f R_p(u_\infty - v) \tag{32}$$

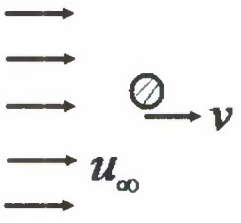

Figure 38: Drag on a spherical particle in a fluid field

Integrating the equation and using v = 0 at t = 0, to find the integration constant, Equation 32 becomes

$$t = \frac{2}{9}\frac{\rho_p R_p^{\ 2}}{\mu_f}\ln\left(\frac{u_\infty}{(u_\infty - v)}\right) \tag{33}$$

Defining the time constant as in Equation 4.3, the above equation becomes Equation 35.

$$\tau = \frac{2}{9}\frac{\rho_p R_p^{\ 2}}{\mu_f} \tag{34}$$

$$\frac{u_\infty - v}{u_\infty} = e^{-t/\tau} \tag{35}$$

At $t = \tau$, $v = 0.63\ u_\infty$. This implies that the particle reaches 63 percent of fluid velocity in τ seconds. The time constant values for different particle diameters with water and PAO as base fluids is shown in Table 6. For the values below, the density of particle used is 774 kg/m^3, and dynamic viscosity of PAO and water used are 4.45×10^{-3} Pa.s and 7.39×10^{-4} Pa.s respectively.

Table 6: Time constant for different particle sizes

Particle diameter (μm)	τ_{water} (ns)	τ_{PAO} (ns)
0.1	0.57	0.09
1	57.5	9.64
5	1437.0	241.0

Governing Equations

With the assumptions mentioned above, the mass and momentum equations for slurry can be written as:

$$\frac{\partial u}{\partial x} + \frac{\partial v}{\partial y} + \frac{\partial w}{\partial z} = 0 \tag{36}$$

$$\rho\left(u\frac{\partial u}{\partial x} + v\frac{\partial u}{\partial y} + w\frac{\partial u}{\partial z}\right) = -\frac{\partial p}{\partial x} + \frac{\partial}{\partial x}\left(\mu\frac{\partial u}{\partial x}\right) + \frac{\partial}{\partial y}\left(\mu\frac{\partial u}{\partial y}\right) + \frac{\partial}{\partial z}\left(\mu\frac{\partial u}{\partial z}\right) \tag{37}$$

$$\rho\left(u\frac{\partial v}{\partial x}+v\frac{\partial v}{\partial y}+w\frac{\partial v}{\partial z}\right)=-\frac{\partial p}{\partial y}+\frac{\partial}{\partial x}\left(\mu\frac{\partial v}{\partial x}\right)+\frac{\partial}{\partial y}\left(\mu\frac{\partial v}{\partial y}\right)+\frac{\partial}{\partial z}\left(\mu\frac{\partial v}{\partial z}\right) \tag{38}$$

$$\rho\left(u\frac{\partial w}{\partial x}+v\frac{\partial w}{\partial y}+w\frac{\partial w}{\partial z}\right)=-\frac{\partial p}{\partial z}+\frac{\partial}{\partial x}\left(\mu\frac{\partial w}{\partial x}\right)+\frac{\partial}{\partial y}\left(\mu\frac{\partial w}{\partial y}\right)+\frac{\partial}{\partial z}\left(\mu\frac{\partial w}{\partial z}\right) \tag{39}$$

The energy equation for the fluid (slurry/pure fluid) is:

$$\rho c_p\left(u\frac{\partial T}{\partial x}+v\frac{\partial T}{\partial y}+w\frac{\partial T}{\partial z}\right)=\frac{\partial}{\partial x}\left(k\frac{\partial T}{\partial x}\right)+\frac{\partial}{\partial y}\left(k\frac{\partial T}{\partial y}\right)+\frac{\partial}{\partial z}\left(k\frac{\partial T}{\partial z}\right) \tag{40}$$

Energy equation for the microchannel wall/fin is:

$$\frac{\partial^2 T_w}{\partial x^2}+\frac{\partial^2 T_w}{\partial y^2}+\frac{\partial^2 T_w}{\partial z^2}=0 \tag{41}$$

The corresponding thermophysical properties of pure fluid and slurry were used for Equations 36 to 40.

Boundary Conditions

For flow inside the channels:

$\mathbf{u} = 0$ at the microchannel and manifold walls, (42)

$p = p_0$, atmospheric pressure at the outlet (43)

$\mathbf{u} = (0, 0, |w|)$ at the inlet (44)

For wall:

$q.n = q_w$; constant heat flux at the base of the fin (45)

$q.n = 0$; adiabatic on all other outer walls (46)

For fluid:

$T = T_{in}$ at the inlet (47)

$q.n = (\rho c_p u T).n$; convective heat flux boundary condition at the outlet/exit, (48)

For wall and liquid interface:

$$T_w = T; \text{ continuity of temperature} \tag{49}$$

$$-k_w \frac{\partial T_w}{\partial n} = -k_f \frac{\partial T_f}{\partial n}; \text{ which is the continuity of heat flux} \tag{50}$$

Dynamic Viscosity

For suspensions that exhibit Newtonian characteristics, the bulk viscosity can be calculated from an empirical formula in terms of the particle concentration. Rutgers [47] has made an extensive survey and has suggested the following correlation by Vand [48, 49].

$$\frac{\mu_b}{\mu_f} = (1 - c - 1.16c^2)^{-2.5} \tag{51}$$

This correlation is derived for spherical particles and is valid for both small and large particle concentrations. In reality, the shape of the encapsulated particles might not be perfectly spherical and hence the viscosity can be different. It can be observed that from Table-1 of [50], the measured experimental viscosity values deviate from the values obtained using Vand's correlation. This difference increases with increase in particle concentration.

3.4b Comparison with Heat Transfer Experiment Results

Heat transfer experiments were performed in MMC heat sinks with an average foot print of 1 cm x 2 cm. There are approximately 441 microchannels inside the heat sink and each channel is approximately is 101 μm wide, 533 μm high and 1 mm long. MEPCM slurry made at BASF was used and consisted of particles of size ranging from 1 to 5 μm with an average diameter of 4.97 μm mixed in water. The core material is n-octadecane and the shell material is polymethylmetacrylate (PMMA). For numerical simulation, viscosity

values provided in [50] were used. The latent melting enthalpy of PCM was measured using differential scanning calorimetry (DSC) and was found to be 120 kJ/kg between 23 ^{0}C and 29 ^{0}C. Properties used for numerical simulation are shown in Table 7.

Table 7: Properties of the suspension components used for experiments

Component	Density, kg/m^3	Specific heat, J/kg.K	Thermal conductivity, W/m.K	Viscosity, kg/m.s	Latent heat, kJ/kg
Water	997	4180	0.604	$1x10^{-3}$	-
MEPCM Particle	867.2	1899	0.1643	-	120
Slurry (10%)	982.3	3951	0.541	$2.3x10^{-3}$	-

Configuration I of Table 5 is used for numerical simulation. Since the average particle diameter is 4.97 μm, the same value was used. Copper is used as the wall material.The flow rate at the microchannel inlet was calculated based on the number of channels and total flow rate at the inlet of the heat sink. The wall thickness of the microchannel was used such that the base heat flux and the total heat supplied is the same as in experiments. In other words, twice the base area in the simulation domain multiplied by number of channels is equal to the base are of the heat sink, which is 2 cm^2. Pressure drop and bulk temperature rise obtained in both cases are presented in Table 8. Pressure drop predicted numerically ranges from 8.3 to 13.0% of total pressure drop obtained in experiments. This suggests that the pressure drop inside manifolds is higher compared to that of pressure drop inside the microchannels, which could be due to poor manifold design. Proper design of the heat sink can result in more than 90% of pressure drop inside microchannels and less than 10% in manifolds. Figure 39 shows the heat transfer coefficient obtained with numerical simulation and comparison with experiment results.

Table 8: Numerical results obtained

Fluid	V_{HS} (GPH)	Q (W)	T_{in}(°C)	ΔT_{bulk}(°C)	ΔP (psi)
Water	5	183.6	22.1	8.5	0.10
Water	10	360.1	33.8	8.3	0.29
Water	15	360.5	34.2	5.8	0.62
Slurry	5	183.6	22.1	8.9	0.18
Slurry	10	360.1	23.6	8.7	0.45
Slurry	15	360.5	25.2	6.1	0.81

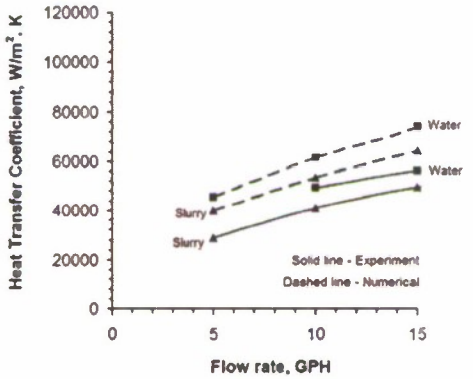

Figure 39: Comparison of numerical and experiment results

The predicted maximum wall temperature using the numerical model does not account for the thermal resistance between the heater surface and the channel wall. Hence, the heat transfer coefficient obtained numerically is higher compared to experiment results. Unstructured mesh was created using the default mesh option in COMSOL and the results were checked for grid independency. The results were found to satisfy the global energy balance at the inlet and outlet of the channel within 4% balance.

Analysis of Experiment Results

The performance of slurry is poorer compared to pure water at all the flow rates. The possible reasons for this behavior of slurry could be due to:

- *Low thermal conductivity of slurry compared to water*

The resultant thermal conductivity of slurry is lower compared to pure water and hence the heat transfer from wall to the fluid in case of slurry is lower.

- *Little or no melting of PCM particles inside the channel*

Since the length of the channel is short for the MMC channel, it is important that the PCM particle completely melts within its residence time. Figure 40 shows the required temperature difference between the fluid and the particle melting temperature for a 5 μm diameter particle at different velocities. A velocity of 0.25 m/s corresponds to V_{HS} = 5 GPH, lowest flow rate used in the experiments. Since the flow is not fully developed thermally, it is highly possible that a large portion of the fluid remained at the inlet temperature and this required temperature difference could not be achieved for all the particles inside the channel.

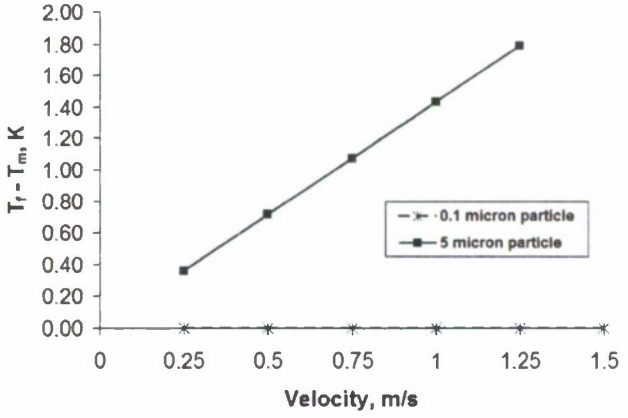

Figure 40: Required temperature difference between particle surface and PCM melting temperature

3.4c Parametric Analysis Results

Based on the above results, it is obvious that the performance of slurry depends on the thermal conductivity of base fluid. Also, the particle size should be smaller so that the particle melts by the time it exits the channel. Since most of the fluid away from the walls did not absorb heat from the walls in case of 101 μm wide channels, simulations were also done in channels of 25 μm width. Parametric study was continued by varying the base fluid, particle concentration and channel dimensions. Table 9 shows the properties of suspension components used.

Table 9: Thermophysical properties used

	Density (kg/m^3)	Specific heat (J/kg.K)	Thermal conductivity (W/m.K)	Viscosity (kg/m.s)	Latent heat (J/kg)
PAO	783	2242	0.143	$4.45x10^{-3}$	-
n-octadecane	815	2000	0.18	-	$244x10^3$
Water	997	4180	0.604	$1x10^{-3}$	-
Copper	8700	385	400	-	-

Performance of water and PAO in 101 μm wide channels

PAO based slurry was used for simulations in channels used for experiment, assuming a particle diameter of 100 nm. The viscosity of the fluid was calculated using Equation 4.26, since there are no reported values of dynamic viscosity for nanoPCM based fluids. For comparison, a heat sink inlet flow rate of 10 GPH and a heat flux of 180 W/cm^2 were used for both water and PAO based fluids. The inlet temperature used is 25 ^0C, which is within the melting range. Figure 41 shows the bulk temperature rise predicted for both water and PAO. It can be observed that the bulk temperature rise decreases with increase in the particle mass concentration. Figure 42 shows the heat transfer coefficient ratio ($h_r = h_{slurry}/h_{purefluid}$) of both water and PAO as base fluid.

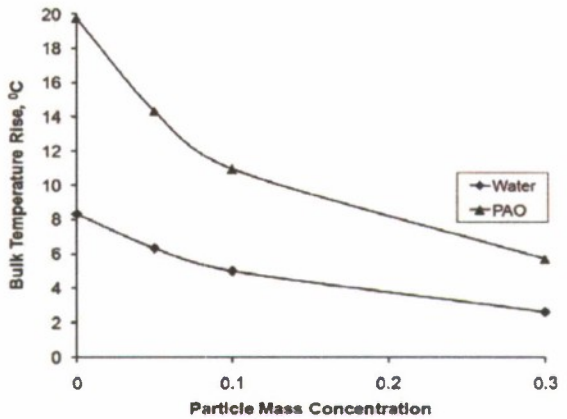

Figure 41: Bulk temperature rise for water and PAO

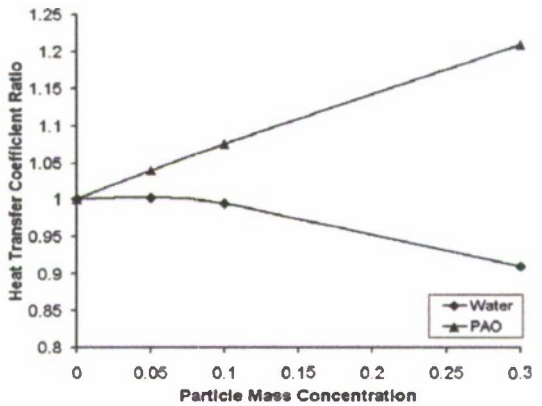

Figure 42: Heat transfer coefficient ratio for water and PAO

In Figure 42, h_{water} = 61832 W/m^2.K and h_{PAO} = 18286 W/m^2.K. The heat transfer coefficient decreases with increase in particle mass concentrations when water is used as the base fluid except with mass concentration equal to 0.05. Slight increase in heat transfer coefficient at mass concentration of 0.05 indicates that the degradation in thermal conductivity is not significant and hence the increase in the specific heat compared to base fluid helps the slurry performance. When PAO is used as base fluid, the heat transfer coefficient increased with increase in concentration. This shows that for developing PCM slurry flows, thermal conductivity plays a very important role in determining the slurry performance.

Performance in 25 μm wide channels

Since most of the fluid did not absorb heat in case of 101 μm wide channels as the thermal boundary layer was not developed, smaller hydraulic diameter was used in order to aid the thermal boundary to develop faster. Hence numerical investigation was continued by using the simulation domain as configuration II (channel width 25 μm). The total number of channels inside the heat sink is 2000. An inlet flow rate of 10 GPH and heat flux of 180 W/cm^2 was used.

Figures 43 and 44 show the temperature profile of water based slurry in both the channels considered. It can be observed that in case of 101 μm wide channels, large portion of fluid did not absorb heat and in case of 25 μm wide channels, the temperature profile is more developed.

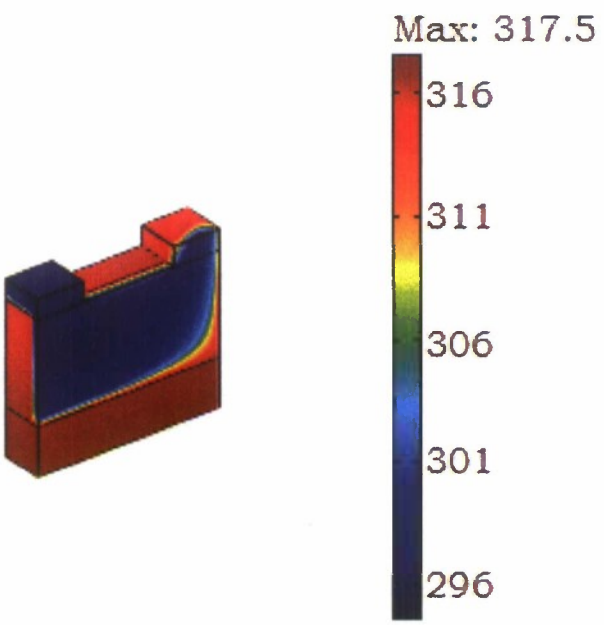

Figure 43: Temperature profile of water based slurry in 101 μm wide channels

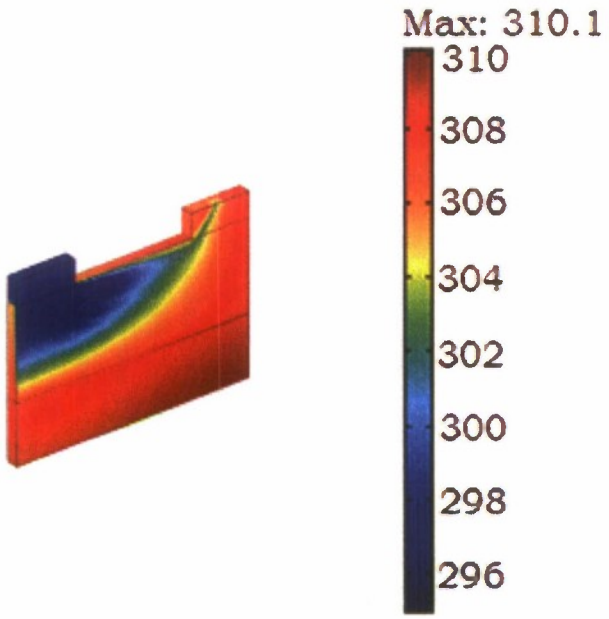

Figure 44: Temperature profile of water based slurry in 25 μm wide channels

Figures 45 and 46 show the bulk temperature rise and heat transfer coefficient ratio predicted with water as base fluid at different fluid inlet temperatures. The heat transfer coefficient of slurry is 1.5 times of water at high mass concentration enabling a maximum wall temperature decrease of 4 K.

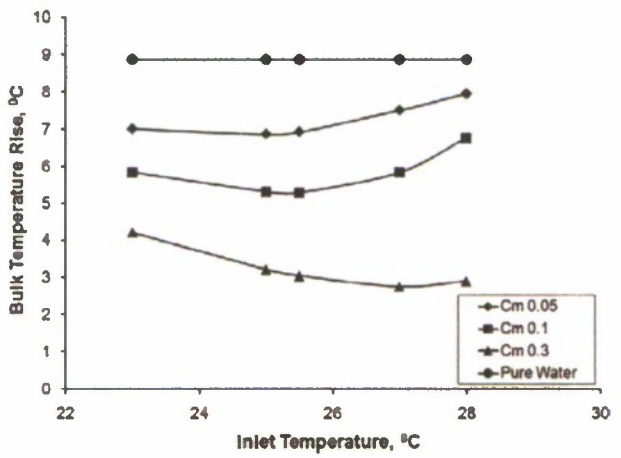

Figure 45: Bulk temperature rise in case of 25 μm wide channels (base fluid – water)

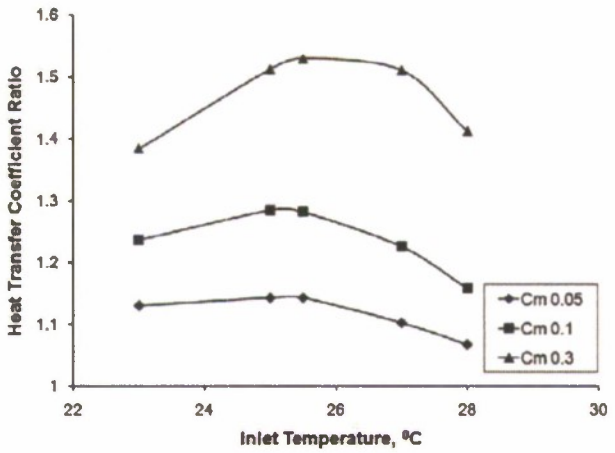

Figure 46: Heat transfer coefficient ratio for water (h_{water} = 150695 W/m^2.K)

Figures 47 and 48 show the bulk temperature rise obtained with PAO as base fluid and the heat transfer coefficient of PAO slurry is twice of pure PAO at high concentration.

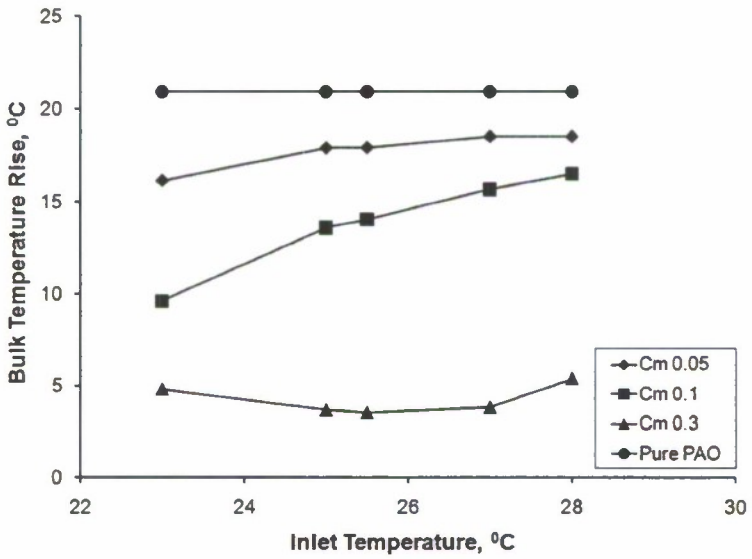

Figure 47: Bulk temperature rise (base fluid – PAO)

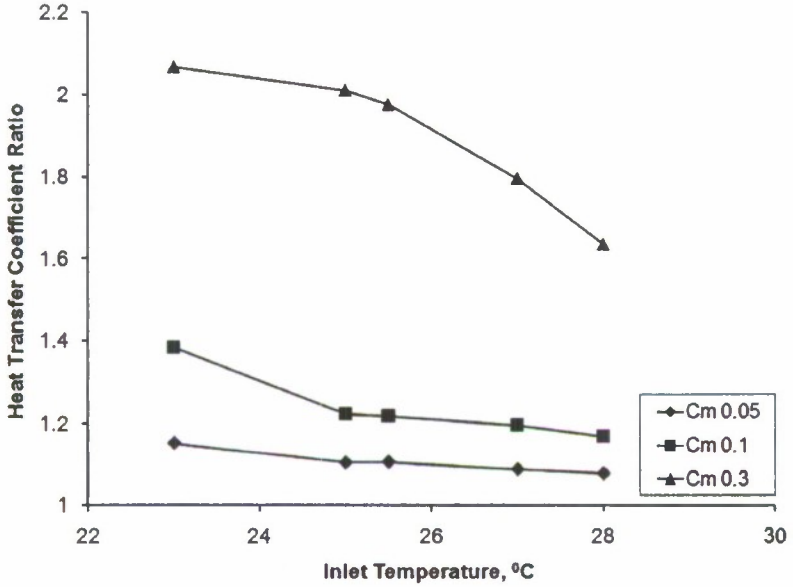

Figure 48: Heat transfer coefficient ratio (Base Fluid PAO, h_{PAO} = 61930 W/m^2.K)

The maximum wall temperature for 30% PAO slurry is 15 K lower than the maximum wall temperature of pure PAO. Decreasing the channel width to 25 μm allow more number of fins within the heat sink. Compared to wider channels, more amount of fluid absorbs heat within each channel and the flow is closer to thermally fully developed as the thermal entrance length is short in case of narrow channels. Hence, using smaller width channels enabling more heat transfer to the fluid helps to obtain better heat transfer coefficient for slurries compared to pure base fluid. Amount of PCM that participates in heat absorption by the time the fluid exits the channel depends on the inlet temperature. For water, if the inlet temperature is around 25.5 ^{0}C, the heat transfer coefficient is the highest, where as for PAO, it is 23 ^{0}C.

Effect of mass concentration on pressure drop

In order to investigate the effect of high concentration on pressure drop, simulations were run using pure water and pure PAO to calculate Performance Factor (**PF**) defined as in Equation 52.

$$\mathbf{PF} = \Delta P_{\text{base fluid}} / \Delta P_{\text{slurry}} \tag{52}$$

This parameter signifies increase or decrease in the pressure drop when a pure fluid is used in order to achieve the same heat transfer coefficient as slurry. For example, the heat transfer coefficient of water based slurry at 5% concentration is 171672 $W/m^2.K$ when the heat sink inlet flow rate is 10 GPH and heat flux is 180 W/cm^2. In order to achieve the same heat transfer coefficient with water, a higher heat sink inlet flow rate was used and the resultant pressure drop inside the channel was 1.14 times of the pressure drop when 5% slurry was used. Figure 49 shows the PF with both water and PAO, when the channel width is 25 μm and heat flux is 180 W/cm^2. The heat sink inlet flow rate used for pure water and PAO is higher than 10 GPH, where as for slurry it is 10 GPH for all the concentrations.

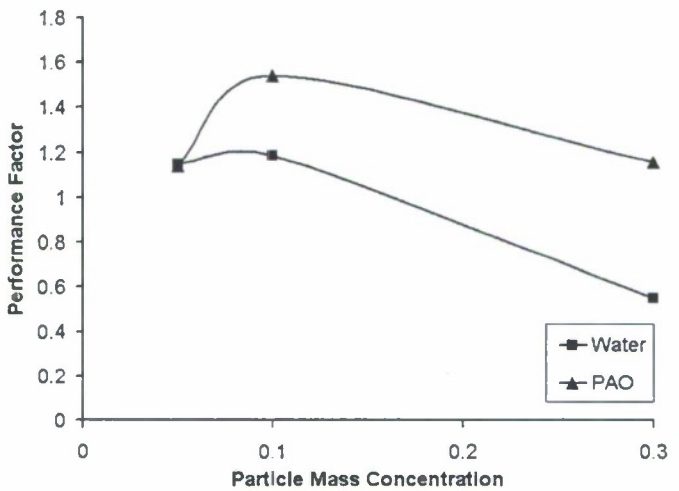

Figure 49: Performance Factor vs c_m

For high mass concentrations, the pressure drop in case of slurry is higher compared to pure water for same heat transfer coefficient. It can be concluded that particle mass

concentration of 0.1 has the highest PF for both water and PAO based slurries. It is assumed that the microchannel pressure drop dominates the total pressure drop. These results are assumed true for the parameters considered and might change with flow rate, channel dimensions, heat flux, fluid inlet temperature etc.

3.4d Conclusion

Thermal conductivity of slurry plays a very important role in the cooling performance of slurry in microchannels, especially in manifold microchannels, which provide flow lengths that are comparable to the developing length of the flow. Results show that the heat transfer coefficient of water based slurry is lower compared to pure water when the channel width is 101 μm. For the same configuration, when the base fluid is changed to pure PAO, that has the thermal conductivity equal to that of the PCM, heat transfer coefficient of slurry is higher compared to pure PAO and the heat transfer coefficient increased with increase mass concentrations. Thus in order to achieve better performance of slurry in developing flows, presence of PCM particles should enhance the thermal conductivity of the base fluid.

Slurry performance depends on the geometric configuration of the microchannel. Numerical investigation showed that in microchannels of width 25 μm, water based slurry too showed high heat transfer coefficient compared to pure water at all mass concentrations. This is possibly because the flow develops faster in smaller channels.

When same heat transfer coefficient is desired with both slurry and water, results showed that higher mass concentrations are not favorable because of large pressure drop across the microchannel. Particle mass concentration of 0.1 showed the highest value of performance factor for the parameters considered.

Performance of PCM slurries in case of thermally developing flows depends on many factors. Using a PCM that can enhance the thermal conductivity of slurry, smaller MEPCM particles that can melt instantaneously, narrow channels that can help the flow develop faster, along with right inlet temperature can help to achieve maximum benefit of slurry and hence tuning of slurry parameters is very important.

SECTION 4: PLANNED ACTIVITIES

The three proposed tasks are completed. In order to analyze the slurry performance in more detail and extend the concept to a wider range of parameters, future work may involve the following:

- Synthesis of nanoPCM particles.
- Perform experiments using nanoPCM slurry in MMC heat sinks.
- Find optimum configuration (right combination of NEPCM particles and fluid, concentration depending on the choice of suspension components, tune inlet temperature and velocity) for obtaining the best thermal performance for a given application.

REFERENCES

1. D.B. Tuckerman, and R.F.W. Pease, High-performance heat sinking for VLSI, IEEE Electron Dev. Lett. 2: 126–129, 1981.
2. L. Zhang, J.-M. Koo, L. Jiang, M. Asheghi, K.E. Goodson, J.G. Santiago, and T.W. Kenny, Measurements and modeling of two-phase flow in microchannels with nearly-constant heat flux boundary conditions, J. MEMS, 0651: 1–8, 2002.
3. S.G. Kandlikar, High flux heat removal with microchannels – a roadmap of challenges and opportunities, Keynote proceedings of the 3rd international conference on microchannels and minichannels, Toronto, Ontario, Canada, June 13-15, 2005.
4. G.M. Harpole, and J. E. Eninger, Microchannel heat exchanger optimization, Proc. 7th IEEE Semi-Ther. Symp: 59-63, 1991.
5. D. Copeland, B. Behnia, and W. Nakayama, Manifold microchannel heat sinks: Isothermal analysis, IEEE Transactions on Components, Packaging, and Manufacturing Technology A, 20: 96-102, 1997.
6. D.P. Colvin, and J.C. Mulligan, Investigation and development of a phase change thermal energy storage system using microencapsulated phase change materials, NASA Phase I final report, May, 1984.
7. D.P. Colvin, and J.C. Mulligan, Microencapsulated phase change for storage of heat, NASA Tech. Brief MFSA-27198, George C. Marshall Space Flight Center, AL, 1987.
8. P. Charunyakorn, S. Sengupta, and S.K. Roy, Forced convection heat transfer in microencapsulated phase change material slurry: flow in circular ducts, Int. J. Heat Mass Transfer, 34: 819-833, 1991.
9. D.P. Colvin, Y.G. Bryant, and J.C. Mulligan, Twenty years of encapsulated PCM development in the United States, Keynote address to the world congress on phase change materials, Geneva, Switzerland, April, 2003.
10. M. Goel, S.K. Roy, and S. Sengupta, Laminar forced convection heat transfer in microcapsulated phase change material suspension, Int. J. Heat Mass Transfer, 37: 593-604, 1994.

11. D.P. Colvin, Y.B. Bryant, J.C. Mulligan, and J.D. Duncan, Microencapsulated phase change heat transfer system, WRDC-TR-89-3072, U.S. Air Force Wright R & D center, OH, 1989.
12. J. C. Maxwell, *A Treatise on Electricity and Magnetism 1, Dover, New York (1954)* vol. 1, 3 ed. New York: Dover Publications, Inc., 1954.
13. C.W. Sohn, and M.M. Chen, Microconvective thermal conductivity of disperse two-phase mixture as observed in a laminar flow, J. Heat Transfer, 103: 45-51, 1981.
14. J.C Mulligan, D.P. Colvin, and Y.G. Bryant, Use of two-component fluids of microencapsulated phase-change materials for heat transfer in spacecraft thermal systems, AIAA paper No.94-2004, 1994.
15. Y. Yamagishi, H. Tahkeuchi, A. Pyatenko, and N. Kayukawa, A Technical evaluation of a microencapsulated PCM slurry as a heat transfer fluid, AIChE Journal, 45(4): 696-707, 1999.
16. Y.-X. Tao, R. Moreno, and Y.L. Hao, Design analysis of a 3-D, ultra-high performance, scalable, micro convective heat sink with NPCM, The first international conference on microchannels and minichannels, Rochester, NY, April 24-25, 2003.
17. Y.L. Hao and Y.-X. Tao, A numerical model for phase-change suspension flow in microchannels, Numerical Heat Transfer A, 46: 44-77, 2004.
18. K.Q. Xing, Y.-X. Tao and Y.L. Hao, Performance evaluation of liquid flow with PCM particles in microchannels, J. Heat Transfer, 127: 931-940, 2005.
19. Segre, G., and A. Silberberg, Behaviour of macroscopic rigid spheres in Poiseuille flow Part 2. Experimental results and interpretation, Journal of Fluid Mechanics, 14:136-157, 1962.
20. P. R. Nott, and J. F. Brady, Pressure-driven flow of suspensions: simulation and theory, Journal of Fluid Mechanics, 275:157-199, 1994.
21. S. Chen and G. D. Doolen, Lattice Boltzmann method for fluid flows, Annual Review of Fluid Mechanics, 30: 329-364, 1998.

22. J. R. Abbott, N. Tetlow, A. L. Graham, S. A. Altobelli, E. Fukushima, L. A. Mondy, and T. S. Stephens, Experimental observations of particle migration in concentrated suspensions: Couette flow, Journal of Rheology, 35: 773-795, 1991.
23. C. J. Koh, P. Hookham, and L. G. Leal, An experimental investigation of concentrated suspension flows in a rectangular channel, Journal of Fluid Mechanics, 266: 1-32, 1994.
24. R. Glowinski, T. W. Pan, T. I. Hesla, and D. D. Joseph, A distributed Lagrange multiplier/fictitious domain method for particulate flows, International Journal of Multiphase Flow, 25: 755-794, 1999.
25. A. W. Chow, S. W. Sinton, and J. H. Iwamiya, Direct observation of particle microstructure in concentrated suspensions during the falling-ball experiment, Journal of Rheology, 37:1-16, 1993.
26. R. J. Phillips, R. C. Armstrong, R. A. Brown, A. L. Graham, and J. R. Abbott, A constitutive equation for concentrated suspensions that accounts for shear-induced particle migration, Physics of Fluids A: Fluid Dynamics, 4: 30-40, 1992.
27. I. M. Krieger, Rheology of monodisperse latices, Advances in Colloid and Interface Science, 3: 111-136, 1972.
28. C. Kim, Mathematical model of migration of spherical particles in tube flow under the influence of inertia and particle-particle interaction, Korean Journal of Chemical Engineering, 21: 27-33, 2004.
29. R. E. Hampton, A. A. Mammoli, A. L. Graham, N. Tetlow, and S. A. Altobelli, Migration of particles undergoing pressure-driven flow in a circular conduit, Journal of Rheology, 41: 621-640, 1997.
30. D. Semwogerere, J. F. Morris, and E. R. Weeks, Development of particle migration in pressure-driven flow of a Brownian suspension, Journal of Fluid Mechanics, 581: 437-451, 2007.
31. A.J.C. Ladd, Numerical simulation of particulate suspensions via a discretized Boltzmann equation, part 1. theoretical foundations, J. Fluid Mech., 271: 285-309, 1994.
32. A.J.C. Ladd, Numerical simulation of particulate suspensions via a discretized Boltzmann equation, part 2. numerical results, J. Fluid Mech., 271: 311-339, 1994.

33. F. Higuera, and J. Jiminez, Boltzmann approach to lattice gas simulations, Europhys. Lett., 9: 663-668, 1989.
34. D.R. Noble, S. Chen, J.G. Georgiadis, and R.O. Buckius, A consistent hydrodynamic boundary condition for the lattice Boltzmann method, Phys. Fluids, 7: 203-209, 1995.
35. B. Chun, and A.J.C. Ladd, Inertial migration of neutrally buoyant particles in a square duct: an investigation of multiple equilibrium positions, Phys. Fluids, 18: 031704, 2006.
36. J.P. Matas, J.F. Morris, and E. Guazzelli, Inertial migration of rigid spherical particles in Poiseuille flow, J. of Fluid Mechanics, 515: 171-195, 2004.
37. E.S. Asmolov, The inertial lift on a spherical particle in a plane Poiseuille flow at large channel Reynolds number, J. Fluid Mech., 381: 63–87, 1999.
38. J.P. Matas, V. Glezer, E. Guazzelli, and J.F. Morris, Trains of particles in finite-Reynolds-number pipe flows, Physics of Fluids, 16: 4192-4195, 2004.
39. D. Leighton and A. Acrivos, The shear-induced migration of particles in concentrated suspensions, *Journal of Fluid Mechanics Digital Archive*, vol. 181, pp. 415-439, 1987.
40. Y. Yamagishi, H. Takeuchi, A. T. Pyatenko, and N. Kayukawa, Characteristics of microencapsulated PCM slurry as a heat-transfer fluid, AIChE Journal, 45: 696-707, 1999.
41. Y. Zhang, X. Hu, and X. Wang, Theoretical analysis of convective heat transfer enhancement of microencapsulated phase change material slurries, Heat and Mass Transfer, 40: 59-66, 2003.
42. L. C. Tao, Generalized numerical solutions of freezing a saturated liquid in cylinders and spheres, AIChE Journal, 13: 165-169, 1967.
43. E. Yamada and K. Takahashi, Effective Thermal Conductivity of Suspensions - 1st Report, Hear Transfer: Japanese Research, 4: 83-101, 1975.
44. E. Alisetti, Forced convection heat transfer to phase change material slurries in circular ducts, M. S. Thesis, University of Miami, 1998.
45. www.comsol.com

46. R. E. Hampton, A. A. Mammoli, A. L. Graham, N. Tetlow, and S. A. Altobelli, Migration of particles undergoing pressure-driven flow in a circular conduit, Journal of Rheology, 41: 621-640, 1997.
47. I. R. Rutgers, Relative viscosity of suspensions of rigid spheres in Newtonian liquids, Rheologica Acta, 2: 202-210, 1962.
48. V. Vand, Theory of viscosity of concentrated suspensions, Nature, 155: 364-365, 1945.
49. V. Vand, Viscosity of solutions and suspensions, J. Phys. Coll. Chem, 52: 300-321, 1948.
50. Y. Rao, F. Dammel, P. Stephan, and G. Lin, Convective heat transfer characteristics of microencapsulated phase change material suspensions in minichannels, Heat and Mass Transfer, 44: 175-186, 2007.